Coastal current convergence structures in the Bay of Biscay from optimized high-frequency radar and satellite data

S. Bertin [a,b,*], A. Rubio [b], I. Hernández-Carrasco [c], L. Solabarrieta [b], I. Ruiz [b], A. Orfila [c], A. Sentchev [a]

[a] Université du Littoral Côte d'Opale, Laboratoire d'Océanologie et de Géosciences, LOG, UMR 8187, Wimereux, France
[b] AZTI, Marine Research, Basque Research and Technology Alliance (BRTA), Pasaia, Gipuzkoa, Spain
[c] Institut Mediterrani d'Estudis Avançat (IMEDEA), Esporles, Illes Balears, Spain

HIGHLIGHTS

- Southeastern BoB exhibits small-scale structures efficiently aggregating particles.
- OI merges drifter and HFR data, aiding CCS research and identification.
- FSLE are valuable to study CCS, but highly reliant on underlying Eulerian fields.
- Backward-in-time FSLE ridgelines delimit the spatial distribution of Chl-a.

GRAPHICAL ABSTRACT
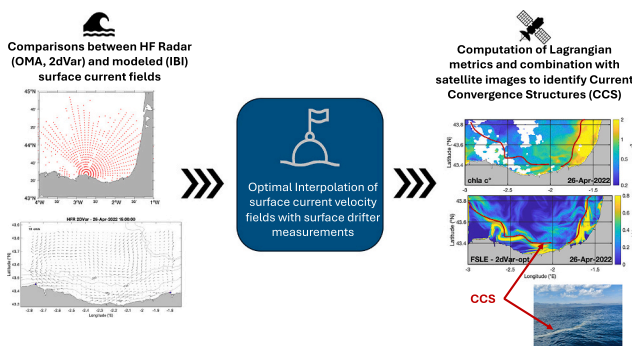
ARTICLE INFO

ABSTRACT

The southeastern Bay of Biscay has been described as a "dead end" for floating marine litter, often accumulating along small-scale linear streaks. Coastal Current Convergence Structures (CCS), often associated with vertical motions at river plume edges, estuarine fronts, or other physical processes, can be at the origin of the accumulation. Understanding the formation of CCS and their role in the transport of marine litter is essential to better quantify and to help mitigate marine litter pollution. The Lagrangian framework, used to estimate the absolute dispersion, and the finite-size Lyapunov exponents (FSLE), have proved very effective for identifying CCS in the current velocity field. However, the quality of CCS identification depends strongly on the Eulerian fields. Two surface current velocity data sets were used in the analysis: the remotely sensed velocities from the EuskOOS High-Frequency Radar (HFR) network and velocities from three-dimensional model outputs. They were complemented by drifting buoy velocity measurements. An optimization method, involving the fusion of drifting buoys and HFR velocities is proposed to better reconstruct the fine-scale structure of the current velocity field. Merging these two sources of velocity data reduced the mean Lagrangian error and the Root Mean Square Error (RMSE) by 50 % and 30 % respectively, significantly improving velocity reconstruction. FSLE ridgelines obtained from the Lagrangian analysis of optimized velocities were compared with remotely sensed concentrations of Chlorophyll-a. It was shown that ridgelines control the spatial distribution of phytoplankton. They fundamentally

represent the CCS which can potentially affect marine litter aggregation. Analysis of the absolute dispersion revealed large stirring in the alongshore direction which was also confirmed by spatial distribution of FSLE ridgelines. The alignment between FSLE ridgelines and patterns of high Chlorophyll-a concentration was observed, often determining the limits of river plume expansion in the study area.

1. Introduction

Extensive research has been devoted to the study of the transport and spatial distribution of particulate material such as pollutants, radioactive isotope markers, algae or marine litter, at large scales (Budyansky et al., 2015; Chenillat et al., 2021). Most of these works focus on the presence of macro-scale CCS, such as subtropical gyres that exhibit remarkable persistence over time (Cózar et al., 2021, 2014; van Sebille et al., 2020, 2015) or the transport of particulate material and connectivity patterns at basin scales, in regions like the northern Iberian waters and the Mediterranean sea (Pereiro et al., 2019; Zambianchi et al., 2017). Some basins, dominated by large-scale open ocean processes and particularly by Ekman dynamics, have been identified as convergence regions for floating marine litter (van Sebille et al., 2020). Indeed, it was estimated that approximately half of the global floating marine litter is concentrated within these hotspots (Kershaw, 2016), emerging the concept of the 7th continent of plastic. However, global distribution and surface-transport mechanisms of floating marine litter are still a long-standing puzzle largely determined by the object's characteristics (like buoyancy and sizes of litter items) (Morales-Caselles et al., 2021).

At mesoscale (i.e. spatial scales from ten to hundreds of kilometers), previous studies focused on the convergence of passive particles in eddies with lifetimes ranging between few weeks to few months (Lebreton et al., 2018; van Sebille et al., 2020). Mesoscale eddies have the capacity to retain particulate material such as radioactive isotope markers (Budyansky et al., 2015) or marine wildlife (Berline et al., 2013; Johnson et al., 2005), and their drift can lead to the transport of passive particles over thousands of kilometers. At sub-mesoscale (i.e. spatial scales under ten kilometers), the study of transport processes is a challenge due to the small size and ephemeral nature of the associated structures, while these processes are known to play a crucial role in the transport and dispersion of particles (McWilliams, 2019, 2016; Poje et al., 2014). Sub-mesoscale fronts, filaments, and vortices provide a fast and efficient route of particulate material transport within the mixed layer (Suaria et al., 2022) and can be associated to several mechanisms such as tides, slope current and shelf-break interactions, upwelling/downwelling, river plumes, eddies or internal waves (Ayouche et al., 2020; Mann and Lazier, 2005). The intense convergence of horizontal flow induced by the sub-mesoscale dynamics can impact the distribution of buoyant material, thereby trapping or collecting floating material as shown in D'Asaro et al. (2018), Huntley et al. (2015) and Hernández-Carrasco et al. (2018a).

CCS have the capacity to concentrate various particulate material, including marine litter (Cózar et al., 2021), larvae, algae, and organic matter such as phytoplankton (Hernández-Carrasco et al., 2018a). The accumulation in CCS can enhance biological productivity, increasing the chance of litter ingestion or entanglement, in line with what is discussed in Gove et al. (2019). Our understanding of ocean currents can help in determining the pathways and fate of floating marine litter, facilitating the prediction of accumulation areas driven by CCS and guiding policy actions to mitigate the impacts of marine litter. In addition, improving our comprehension of processes inducing CCS and their impact on the transport of particulate material by ocean currents is essential in physical oceanography, as these particles can serve as pathways indicator for understanding ocean circulation at sub-mesoscale.

In the southeastern Bay of Biscay (hereinafter BoB), coastal waters are considered as accumulation zone for floating marine litter (Pereiro et al., 2019; Rodríguez-Díaz et al., 2020). Coastal currents are highly influenced by seasonal variations, with weaker currents during the

spring and summer months, leading to higher retention of particulate material (Declerck et al., 2019). In the observation-based study of Ruiz et al. (2020), CCS with large accumulation of floating material were documented. These CCS, referred to by the authors as "marine litter windrows" are identifiable to the naked eye as rectilinear lines parallel to the coast spanning over one kilometer in length. They are found to concentrate 10^4 more marine macrolitter items than the surrounding waters (Ruiz et al., 2020; Basurko et al., 2022).

For better understanding the processes underlying the formation of CCS, often visible in the BoB, it is necessary to improve the capability of detection of these phenomena from observational data. Surface fronts are commonly detected by satellites using infrared and microwave sensors (Prants, 2022). Identification can me made based on the calculation of gradients by detecting rapid changes in the physical properties of water, such as temperature, salinity or density (Belkin and O'Reilly, 2009; Chapman et al., 2020; Xing et al., 2023; Zainuddin et al., 2006). However, these techniques are limited by the spatial resolution of the satellite images and by the presence of cloud cover. In the Lagrangian framework, and when surface currents at the desired spatio-temporal resolution are available, surface fronts can be detected by computing the Lagrangian Fronts, maximum of Lagrangian indicators (Prants et al., 2014a, 2014b). Lagrangian indicators correspond to functions of trajectory of a single fluid particle such as finite-size Lyapunov exponents (FSLE, d'Ovidio et al., 2004; Della Penna et al., 2017; Hernández-Carrasco et al., 2011; LaCasce, 2008). In this study, we propose to adopt a Lagrangian approach based on the computation of absolute dispersion (Berti et al., 2011; Bouzaiene et al., 2020; Davis, 1983; Enrile et al., 2019) and FSLE using surface current velocity fields from observation and modelling.

Backward-in-time FSLE are used to investigate mixing, transport pathways, and to identify attracting Lagrangian Coherent Structures (aLCS) (d'Ovidio et al., 2004; Hernández-Carrasco et al., 2011). Ridgelines of backward-in-time FSLE correspond to aLCS (Hernández-Carrasco et al., 2018a) where surrounding Lagrangian trajectories converge. Hence, ridgelines of aLCS can be used as a proxy of Lagrangian convergence regions (Hernández-Carrasco et al., 2018a; Huntley et al., 2015), where larger concentration of marine litter is likely to occur. While FSLEs and aLCS seem appropriate for identifying regions with potential floating marine litter concentration, their capacity to accurately identify CCS locations and characteristics strongly relies on the underlying Eulerian fields used to estimate these Lagrangian quantities. Even more crucial is the application of these techniques in coastal areas, where dynamics are inherently complex. The majority of research has predominantly concentrated on the open ocean, with fewer studies reporting on the use of these methods in coastal regions. (Ghosh et al., 2021; Suara et al., 2020).

The aim of this study is to improve the efficiency of the CCS identification in the southeastern BoB, by the fusion of data from HFR surface velocity measurements and Lagrangian drifters, assessed against Chlorophyll-a (Chl-a) satellite images. Using the best representation of CCS from optimized HFR data, and Lagrangian diagnostics directly computed from the in-situ Lagrangian drifters, the characteristics of CCS in the area are described for two different periods of time under contrasting hydrodynamic conditions.

2. Study site and hydrodynamic conditions

The coastal circulation in the southeastern BoB has a complex pattern. Along the slope, the Iberian Poleward Current, a regional

component of the North Atlantic Eastern Boundary Current System, flows eastward, along the Spanish coast, and northward, along the French coast. It exhibits a relatively intense northward flow (0.4–0.7 m/s at the surface) during late autumn and winter, while the flow weakens and becomes more variable, moving mostly eastward in summer (Charria et al., 2013; Rubio et al., 2019; Solabarrieta et al., 2014).

On the shelf, the circulation is primarily driven by seasonal variations in winds (González et al., 2004; Solabarrieta et al., 2015). Autumn and winter are affected by prevailing southwesterly winds that reinforce the northward flow, while spring and summer bring northeasterly winds, resulting in a weaker and highly variable eastward flow. Due to the narrow shelf and relatively low river discharges, wind-driven currents dominate tidal or density-driven currents over the shelf (González et al., 2004; OSPAR Commission, 2000). The Adour River is the primary source of runoff (Ferrer et al., 2009), supplemented by the Gironde River, located 170 km north of the study area, and much weaker river runoff sources along the Spanish coast. Persistent mesoscale eddies are recurrently triggered by the interaction of the Iberian Poleward Current with the abrupt bathymetry, a phenomenon well-documented in previous studies (e.g. Pingree and Le Cann, 1992; Rubio et al., 2018). As a result, transport and retention conditions at the surface exhibit interannual, seasonal, and daily variability, influenced by general circulation, wind-driven currents, *meso*scale structures, and fronts (Rubio et al., 2020). Shorter time-scale variability is caused by tidal and inertial motions (Rubio et al., 2011).

The region faces several pressing concerns, which extend to the broader BoB area. These include pollution from hazardous substances near urban and industrial areas such as Bilbao and San Sebastian, the rising incidence of toxic algal blooms causing eutrophication, biodiversity loss, and the proliferation of invasive species (Borja et al., 2019). The southeastern BoB has been identified by global and regional models as an accumulation zone for marine litter (Pereiro et al., 2018; Rodríguez-Díaz et al., 2020). Recent studies on both macrolitter (Ruiz et al., 2020; Basurko et al., 2022), microlitter at the water surface, and biota (Davila et al., 2021) have shed a light on litter quantities and behaviors within the BoB. These recent studies emphasize the hypothesis of the Bay being an accumulation zone and they also highlight its large seasonal variability (Declerck et al., 2019; Pereiro et al., 2019; Ruiz et al., 2022).

The existence of the EuskOOS HFR network in the study area, in combination with numerical model outputs and satellite data, provides extensive historical and near real-time information on the regional ocean-meteorological conditions. It also offers opportunities for the development of Lagrangian studies at meso and upper sub-mesoscale levels, particularly in areas where CCS act as barriers to transport of particulate material.

3. Data and methods

3.1. Current velocity from surface drifters and ADCP

Two in-situ surveys were conducted in coastal waters of the southeastern BoB: the BOBLIT0.1 survey in spring (hereinafter referred to as S1) and the BOBLIT0.2 survey in autumn (hereinafter referred to as S2). Both surveys were conducted in the same geographical area, where occurrence of coastal CCS had been reported. During S1, from April 26th 11:45 UTC to 28th April 07:00 UTC, 13 surface drifters were deployed in three different clusters (Fig. 1, red dots), within visible CCS where qualitative aggregation of foam and macrolitter items was observed (Fig. 2). Three drifters were deployed in a longitudinal transect at −2.4°E in cluster 1 (Fig. 1b), five other drifters were deployed in cluster 2 (Fig. 1 b) centered at 43.4°N, −2.25°E and the last five were deployed in cluster 3 centered at 43.35°N, −2.3°E. The mean separation distance between drifters was 10, 1.7 and 0.6 km in clusters 1, 2 and 3 respectively.

During S2, conducted from October 24th 14:00 UTC to October 28th 03:00 UTC, no visible CCS were present. Thus, nine Lagrangian drifters were deployed in a rectangular area (15 km long and 12 km wide), with an initial separation of 3 km between drifter pairs (Fig. 1b). In addition to surface drifters, the surface layer velocities (1 m below the sea surface) were measured using a towed Acoustic Doppler Current Profiler (ADCP, RDI 600 kHz) transect survey, conducted during S2. The ADCP track lasted a total of four hours with a sampling frequency of 1 min and covered an area of 9 km × 6 km, in the southern part of the domain (43.3°N, 2.3°E, Fig. 1b – green trajectory).

For consistency, the subsequent analysis covers 40 h period of time starting at the beginning of each survey.

Three types of drifters were used: the coastal Nomad surface buoys, cylinder-shaped manufactured by SouthTek (https://www.southteksl.com/), ODI surface buoys formerly manufactured by Albatros Marine Technologies, and a set of cylinder-shaped home-made drifters (whose design was similar to the coastal Nomad drifters). All drifters were equipped with an anchor of 0.5 m long positioned in the water column between 0.8 and 1.3 m depth, allowing them to drift with surface currents. Observed surface current velocities were estimated from drifter trajectories with a timestep of 15 min, nominal period of drifter positioning via GPS. Potential differences in behavior between different drifter designs were neglected in the Lagrangian computation of absolute dispersion and Lagrangian errors, taking into account the short-term window considered (40 h). For the optimization of the Eulerian fields with the Optimal Interpolation (OI) method, the uncertainty associated to the different drifter designs was parametrized using an observational error equal to 0.05 m/s (see Section 3.6).

3.2. Current velocities from HFR

Hourly surface velocity current fields were obtained from the EuskOOS HFR network, consisting of two CODAR Seasonde stations located along the Spanish Basque Country coast in the southeastern BoB (Fig. 1). EuskOOS HFR network (https://doi.org/10.57762/T4WH-DQ48) is a part of JERICO-RI (https://www.jerico-ri.eu/) and it is operated following JERICO-RI standards and recommendations (Mantovani et al., 2020; Rubio et al., 2018; Solabarrieta et al., 2016). The two individual radar stations, operating at a frequency of 4.86 MHz, enable velocity measurements within the range of up to 200 km with 5 km along-beam resolution, and 5° angular resolution. Velocity data are obtained at 1 h time step and distributed as part of Copernicus Global Ocean- in-situ near real- and delayed-time surface ocean currents products (http://doi.org/10.48670/moi-00041& http://doi.org/10.17882/86236).

Using the measured radial velocities, two products of total surface current velocities fields were generated, covering the area from −3°E to −1.3°E and from 43.3°N to 44°N. On one hand, the open-boundary modal analysis (OMA, Kaplan and Lekien, 2007) gap-filling method was applied to the HFR radial velocities (Table 1) to obtain hourly OMA current fields with 5 km spatial resolution, during the periods of April–May 2022 and October–November 2022. Only OMA values with the geometric dilution of precision (GDOP) errors below the threshold of 8 cm/s (Solabarrieta et al., 2014) were considered for this study.

On the other hand, the two-dimensional variational interpolation method (2dVar, Yaremchuk and Sentchev, 2009) was applied to HFR radial fields (Table 1) to obtain hourly 2dVar current fields with 2.5 km spatial resolution. 2dVar is a non-local and kinematically constrained interpolation method which generates surface current velocity maps by using a combination of all measured velocities, within a given grid, reconstructing the velocity vector in one location. Estimations of the relative error of interpolation were computed at each time step. 2dVar fields were computed for an extended period from January 2020 to December 2022, since they were also used as historical input for the optimization method. To ensure that the method effectively captured
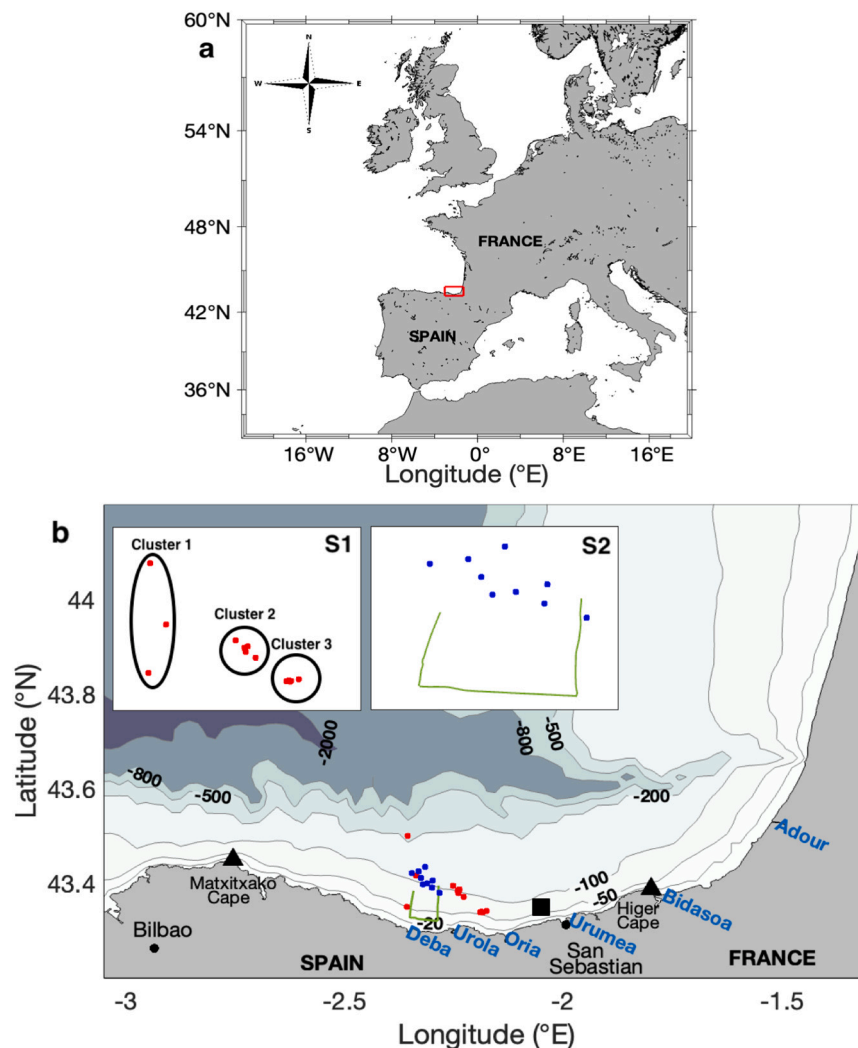
Fig. 1. (a) Study area in the southeastern BoB, represented by the red rectangle. (b) Map and details of the study area. Bathymetry is shown by blue shading. Black triangles show the two HFR stations located at Matxitxako and Higer Capes. The location of major rivers is given in blue. Geographic names used in the text are also shown. Red and blue dots show the release location of drifters during S1 and S2 surveys, respectively, and are presented in a zoom in the upper part of the figure. The ADCP transect conducted during S2 is shown by the green trajectory.

the information derived from the available radial velocities, a careful consideration was given generating the grid for performing the 2dVar interpolation. On average, there were 870 observations collected every hour, with the mean distance of about 5 km between observations within the study area. For this study, we opted for a 2dVar grid consisting of 1500 interpolation points, establishing a 2:1 ratio between the number of observations and the number of interpolated points, in coherence with the 2:1 ratio between the average distance between observations and the grid resolution. The 2dVar method was applied with a noise level set to 0.06 m/s.

3.3. Current velocities from IBI model

Model surface current velocities were obtained from the Iberia-Biscay-Ireland (IBI) product (Table 1) provided by the Copernicus Marine Environment Service (CMEMS, doi:10.48670/moi-00027). IBI is a product that covers the northwestern European waters, based on an eddy-resolving three-dimensional NEMO configuration, with a time-space resolution of 15 min and 1/36°. The model is forced with 3-hourly atmospheric fields provided by ECMWF. Lateral open boundary conditions (temperature, salinity, velocities, and sea level) are interpolated from the daily outputs from the MyOcean Global eddy resolving system.

Tidal boundary conditions were obtained from the global tide models FES2004 (Lyard et al., 2006) and TPXO7.1 (Egbert and Erofeeva, 2002). Freshwater river discharge inputs are implemented as a lateral open boundary condition for 33 rivers with flow rates based on observations and climatology data. The bottom topography is taken from the GEBCO08 dataset (Maraldi et al., 2013). IBI does not include data assimilation (Mason et al., 2019). The velocity data were extracted from the model outputs within the region of interest defined above.

3.4. Wind and satellite data

Wind data were obtained from the Weather Research and Forecasting model (WRF) provided by the meteorological agency of Galicia. The description of the model is detailed in (Skamarock et al., 2019). In this study, hourly zonal and meridional components of wind velocity at a height of 10 m were used, featuring a spatial resolution of 12 km, covering the predefined geographic area.

Remotely sensed surface Chl-a estimates were obtained from the CMEMS catalogue (doi:10.48670/moi-00286). This product derives from the Sentinel-3 Ocean and Land Color Imager (OLCI) spectrometer. The Chl-a concentration used is OC4Me, corresponding to the pigment concentration based on the ocean color algorithm developed for MERIS,
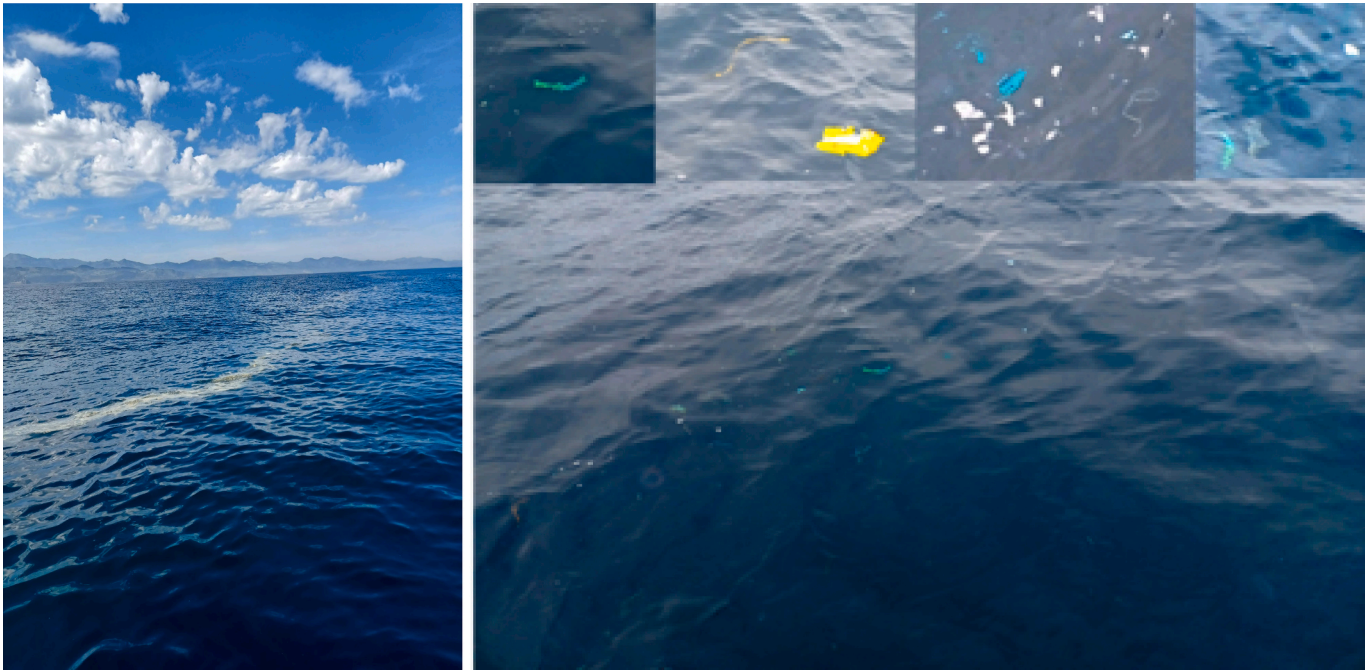
Fig. 2. Photos of one of the coastal CCS observed during S1 survey, where drifters were deployed (easternmost cluster). Aggregation of foam and macrolitter was observed, although not quantified.

and following the approach of O'Reilly et al. (1998), with a spatial resolution of 300 m and a temporal resolution of one day. The Chl-a concentration product used is cloud polluted. Although various algorithms exist to fill the data gaps below clouds (e.g., Stock et al., 2020), these methods generally require much longer time series of Chl-a images, which results in smother fields, and are not the best suited to study CCS during the short-time periods of S1 and S2 surveys.

3.5. Estimation of Lagrangian trajectories and Lagrangian error

Virtual trajectories were computed using the open-source Lagrangian framework OpenDrift (https://opendrift.github.io/, see Dagestad et al., 2018; Jones et al., 2016) and the different surface current fields (Table 1). Virtual drifters were seeded at the time and location of the real drifters every hour, and advected using the 4th order Runge-Kutta scheme and bilinear interpolation. The horizontal diffusion parameter was set to 0. The accuracy of virtual trajectories was assessed using the Lagrangian error ε_L (Liu and Weisberg, 2011; Ruiz et al., 2022). The estimation of ε_L involves the computation of the separation distance between the location of the real drifter and that of virtual drifter moving in the velocity field.

Considering d_{tk}, the separation distance between the real and the k-th simulated trajectory at time step t, the Lagrangian error is computed at each time step and averaged over all the simulated trajectories corresponds to each real drifter trajectory, following the expression:

$$\varepsilon_L(t) = \left\langle \sum_{t=1}^{N} \sum_{k=1}^{N-(t+1)} \frac{d_{tk}}{N-(t+1)} \right\rangle \tag{1}$$

with N corresponding to the maximum number of time steps of drifter displacement, which is also equal to the number of simulated trajectories. The Lagrangian error calculation schema is shown in Appendix A.

To facilitate comparisons, the Lagrangian error was divided by the mean drift distance of the real drifters (travel distance averaged over all the drifters), giving rise to a dimensionless index L.

The Lagrangian error calculation also included the estimation of the travel distance and separation distance (distance between the real drifter trajectory and the virtual drifter trajectory) of each available surface current field at each time step, considering only the virtual particle deployed at the initial time.

3.6. Optimal interpolation of drifter velocity measurements

Optimal Interpolation (OI) was used to merge current velocities obtained from drifting buoy trajectories and 2dVar HFR velocities, resulting in the optimized 2dVar surface current product (hereinafter 2dVar-opt). Following a meticulous assessment of the accuracy of the various available surface current products (refer to Table 1), 2dVar was chosen for optimization due to its higher performance, as discussed in Section 4.1.

By performing a weighted least-squares fit of a background field to the drifter velocities, this method can provide a better estimation of the state of ocean dynamics. OI is generally used when observations are available at irregularly distributed points and are assumed to be affected by an observation error, e.g., drifter measurements. This observation error is assumed to be uncorrelated with 2dVar HFR fields error and is set to 0.05 m/s, which is twice the uncertainty due to drifter positioning. This adjustment ensures that potential errors attributed to the various buoy designs used in sea surveys are adequately accounted for.

Table 1
Characteristics of the surface current fields used in the study for computation of Lagrangian error, absolute dispersion and FSLE.

Short name	Spatial resolution (km)	Temporal resolution (h)	Description
OMA	5	1	HFR computed with OMA method from radial hourly surface current velocity field, provided by CMEMS.
2dVar	2.5	1	HFR computed with 2dVar method from radial hourly surface current velocity field, provided by CMEMS.
2dVar-opt	2.5	1	2dVar fields optimized with measurements of surface current velocity by surface drifters through OI (described Section 3.6)
IBI	3	0.25	Model data provided by CMEMS.

OI provides a correction of a background velocity field $\boldsymbol{u}_r(\boldsymbol{x}, t)$ by performing a linear combination of the weighted differences between the background trajectory $\boldsymbol{u}_r$, and the observed drifter velocities $\boldsymbol{u}_i^*$ at point i (Sentchev and Yaremchuk, 2015). Weights chosen for minimization of the mean square difference between drifter and HFR velocities are a combination of 2dVar HFR ($\boldsymbol{B} = \langle \boldsymbol{u}_r(\boldsymbol{x}, t) \boldsymbol{u}_r(\boldsymbol{x}', t') \rangle$) and drifter ($\boldsymbol{R}_{ij} = \langle \boldsymbol{u}_i^*(\boldsymbol{x}, t) \boldsymbol{u}_j^*(\boldsymbol{x}', t') \rangle$) velocity covariances. The optimized velocities $\boldsymbol{u}_{opt}$ at radar grid are computed as follows:

$$\boldsymbol{u}_{opt} = \boldsymbol{u}_r + \sum_{ij} \boldsymbol{B} \boldsymbol{H}_j^T \left(\boldsymbol{H}_i \boldsymbol{B} \boldsymbol{H}_j^T + \boldsymbol{R}_{ij} \right)^{-1} \left(\boldsymbol{H}_i \boldsymbol{u}_r - \boldsymbol{u}_i^* \right), \tag{2}$$

where $\boldsymbol{H}_i$ corresponds to a linear operator projecting gridded velocity values from the apexes of the radar grid cell onto the ith observation point location.

The performance of each velocity field, and particularly the quality of the interpolation scheme, is quantified by estimating the Root Mean Square Error (RMSE), corresponding to the mean relative difference between the drifter velocities $\boldsymbol{u}^*$ and the desired velocity field $\boldsymbol{u}$ as follows:

$$RMSE = \sqrt{\sum_i \left(\boldsymbol{H}_i \boldsymbol{u} - \boldsymbol{u}_i^* \right)^2}. \tag{3}$$

The success of OI relies on the background field, which should ideally be a close approximation to the truth. Nonetheless, the outcome is also linked to the composition of the covariance matrix, comprising a large number (80) of 40-h long trajectories known as ensemble members. These ensemble members are expected to represent similar circulation patterns as those observed during the survey (background current velocities and tidal phase).

For selecting ensemble members, the non-linear K-Means clustering algorithm (Hastie et al., 2009; Solabarrieta et al., 2015) is employed to analyze 2dVar HFR derived velocities from January 2020 to December 2022. The primary objectives of using this method are twofold: (i) to identify and categorize the dominant surface current groups present during both survey periods, and (ii) to extract ensemble members with similar dominant groups in the extended time series data, which are subsequently used to create the covariance matrix required for OI. The K-Means algorithm employs a fixed number of clusters, which was set to 12, with further details provided in Appendix B. Additionally, the number of ensemble members used was set to 80. Sensitivity tests on the number of ensemble members to OI results are presented in Appendix B.

An additional assessment of the performance of the 2dVar reconstruction using the given approach was completed by the comparison of the results with real trajectories (see Section 4.1) and by the examination of the interpolation errors with time and as the function of the number of available HFR observations (not shown). Although the relative error of 2dVar interpolation is sometimes relatively large (up to 0.7), it shows an overall mean of 0.5 during S1, and 0.4 during S2. During S1, the evolution in time of the interpolation error was found to be inversely proportional to the number of available HFR observations, with a correlation coefficient between the interpolation error and the number of available observations of -0.5. However, this was not the case during S2 where both quantities were found uncorrelated (correlation coefficient equal to -0.2). This difference can be explained by the different dynamics observed during the two campaigns. During S1, surface current velocities were low and featured numerous eddies, more difficult to measure accurately by HFR, which explains the correlation between the number of observations and the 2dVar error. On the other hand, during S2, surface current velocities were driven by a strong coastal jet, much easier to measure by HFR, even in situations when the number of observations is not optimal.

3.7. Lagrangian metrics to estimate spreading and convergence of trajectories

The absolute (cluster) dispersion $A^2(t)$ is generally used to quantify the intensity of the particle spreading induced by the surface current field. $A^2(t)$ is defined as the variance of particle spreading with respect to the mean coordinate of particles in a cluster (the barycenter). In two-dimensions, the dispersion can be estimated along x and y axis (Berti et al., 2011; Enrile et al., 2019) following the expression:

$$a_{ij}^2(t) = \frac{1}{M} \sum_{m=1}^{M} \left\{ \left[x_i^m(t) - \overline{x_i^m(t)} \right] \left[x_j^m(t) - \overline{x_j^m(t)} \right] \right\} \quad A^2(t) = a_{xx}^2(t) + a_{yy}^2(t). \tag{4}$$

Here, a_{ij}^2 corresponds to the variance along i and j spatial coordinates, a_{xx} and a_{yy} corresponds to the absolute dispersion along x and y respectively, M is the number of drifters, $x^m(t)$ is the position of the m-th drifter at time t and $\overline{x^m(t)}$ is the coordinate of the barycenter.

Estimation of the absolute dispersion allows to identify two fundamental regimes of dispersion in the turbulent flow. At short times, i.e. during the first few hours of the drifter deployment, the growth of absolute dispersion follows generally a ballistic regime corresponding to $A(t)^2 \sim t^2$ (Berti et al., 2011; Bouzaiene et al., 2020; Davis, 1983; Enrile et al., 2019; Poulain and Niiler, 1989; Taylor, 1922). This regime occurs when the pair velocities of the drifters are strongly correlated, influenced by strong and persistent currents such as a coastal jet. At larger timescales, when the memory of the initial condition is lost, and the absolute dispersion can grow as $A(t)^2 \sim t$ (Berti et al., 2011; Bouzaiene et al., 2020; Davis, 1983; Enrile et al., 2019; Poulain and Niiler, 1989; Taylor, 1922), following a random-walk regime of dispersion.

The FSLE technique is used to analyze the ocean transport and mixing (Aurell et al., 1997; d'Ovidio et al., 2004; Hernández-Carrasco et al., 2011; LaCasce, 2008). The largest FSLE values concentrate along characteristic lines, identifying regions of maximum stretching, which corresponds to oceanic structures such as fronts, eddies boundaries, etc. As the aLCS cannot be crossed by particle trajectories, they act as barrier to transport, governing therefore the motion of the surrounding fluid particles around them. FSLE values, given by λ, are estimated as the inverse of the time $\tau(\boldsymbol{x})$ required for two particles of fluid to separate from an initial distance δ_0 to a final distance δ_f, and is expressed at position $\boldsymbol{x}$ and time t as:

$$\lambda(\boldsymbol{x}, t, \delta_0, \delta_f) = \frac{1}{\tau(\boldsymbol{x})} ln\, \alpha = \frac{1}{\tau(\boldsymbol{x})} ln \frac{\delta_f}{\delta_0}. \tag{5}$$

In this study, values of λ were computed using the algorithm described in Hernández-Carrasco et al. (2011) with the amplification factor $\alpha = 8$ in order to measure high stretching as well as to obtain reliable aLCS. The parameter δ_0 is fixed to 0.4 km to capture fine-scale structures. Thus, $\delta_f = \alpha\, \delta_0 = 3.2$ km. Particle trajectories were integrated backward-in-time over 15 days, since the associated aLCS have a direct physical interpretation (i.e. nearby particle trajectories lie along the hyperbolic aLCS). This enables us to understand the fate and pathways of marine litter and identify potential CCS (Hernández-Carrasco et al., 2018a, 2011). A sensitivity test to the number of days of integration and to the amplification factor was conducted. We obtained that 15 days of integration and an amplification factor of 8 were a good choice to obtain reliable aLCS and detect transport barriers.

Note, however, that the drifter trajectories in both experiments had a relatively brief duration of approximately 40 h, providing only 40 h of 2dVar-opt velocity fields. The backward-in-time FSLE at t is computed using backward trajectories from t to $t - 15$ days, relying on the velocity field from t to $t - 15$ days. In instances where the 2dVar-opt does not exist (t inferior to the deployment time), 2dVar velocity field is used for the FSLE calculation.

4. Results

4.1. Optimization of surface current fields for dispersion quantification and CCS identification

Before optimizing the surface velocity fields, an extensive comparison exercise was conducted to assess the capabilities of various available Eulerian fields in reproducing the dynamics observed by drifting buoys (as explained in the previous section). This exercise led to the identification of the 2D Variational horizontal currents (2dVar) solution as the field to be optimized. The following results showcase the comparison of different current fields, including the 2dVar-opt field, with the aim to illustrate how the latter provides the best fit to drifting buoy data.

Above all, the performance of the optimization method was assessed by comparing velocity fields from different datasets with independent velocity measurements. Surface layer velocities (at 1 m depth) from a towed ADCP transect survey, conducted during S2, were used in comparison. The relative error between ADCP velocities and those derived from HFR measurements, interpolated into the ADCP track and sampling frequency, before and after optimization was reduced by a factor of two, from 0.26 to 0.11. In particular, the current direction was considerably improved. Then, other quantities were estimated to show improvements brought by data fusion.

In a qualitative approach, Fig. 3, provides two examples of comparison between real and virtual trajectories computed from the different surface current fields during S1 and S2 surveys. During S1 (Fig. 3a), the 2dvar-opt trajectory closely matches the real one in terms of separation distance, although not in terms of travel distance since it fails to reproduce the amplitude of the loops (due to a combination of tidal and inertial processes) exhibited by the real trajectory. OMA and 2dVar trajectories are mostly rectilinear and follow the 80-100 m isobaths. While the OMA trajectory does not show any loop, the 2dVar trajectories do depict small amplitude oscillations within the first hours after the beginning of the computation. The IBI trajectory is the one that shows the largest separation distance since it is advected in the opposite direction to the real drifter, depicting oscillations with similar amplitude of that of the real trajectory (Fig. 3a).

During S2 survey (Fig. 3b), the mean travel distance covered by the drifter was 68.9 km. In this period, the observed currents were much more intense and less variable, showing all the trajectories a net eastward drift along the 100 m isobath, with exception of the OMA trajectory. The 2dVar-opt trajectory is the closest to observations with a travel distance of 63.3 km. Travel distances are overestimated regarding IBI and 2dVar trajectories and underestimated regarding OMA trajectory. The 2dVar-opt trajectory follows the 100 m isobath, with very small separation distances from the real trajectory through all the paths. IBI and OMA trajectories show the worst fit.

Different statistics for real surface drifters during S1 and S2 surveys and the different current fields are presented in Table 2. Mean and maximum velocity values, mean travel distances, L index and RSME are computed from real and virtual trajectory pairs. Regarding mean velocity, all velocity fields yield similar results for S1 and S2 and are in accordance with the values measured by surface drifters. However, there is typically a visible difference of 0.1 m/s in maximum velocity when comparing these values with the data from surface drifters (Table 2). During S1, all the surface current fields underestimate the maximum velocity measured by the drifters by 0.1 m/s. During S2, 2dVar and IBI underestimate the maximum velocity by 0.1 m/s while OMA and 2dVar-opt give the same results as drifter measurements.

Table 2
Mean and maximum current speed, the average travel distance calculated from all the pairs of real and virtual trajectories pairs. *L* index and RMSE calculated using the OMA, 2dVar, IBI and 2dVar-opt fields.

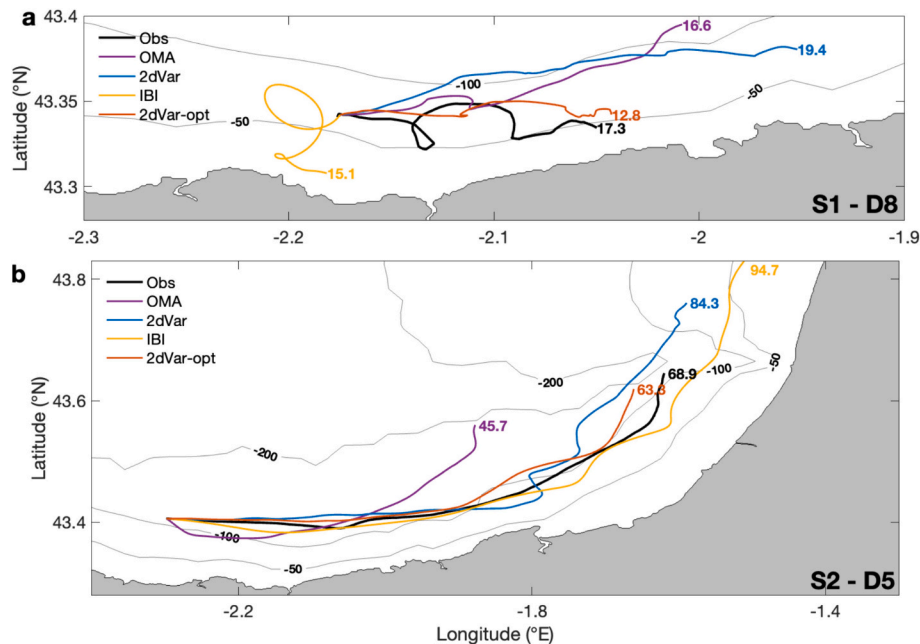|		Drifters	OMA	2dVar	IBI	2dVar-opt
Mean velocity (m/s)	S1	0.1	0.1	0.1	0.1	0.1
	S2	0.3	0.3	0.3	0.3	0.3
Max velocity (m/s)	S1	0.3	0.2	0.2	0.2	0.2
	S2	0.5	0.5	0.4	0.4	0.5
Mean travel distance (km)	S1	19.5	16.7	14.6	18.4	12.9
	S2	62.0	46.3	80.0	95.6	61.0
L index	S1	–	0.6	0.5	0.7	0.3
	S2	–	0.3	0.2	0.3	0.1
RMSE	S1	–	1.3	0.9	1.4	0.7
	S2	–	0.6	0.4	0.5	0.3

Fig. 3. Real and virtual drifter trajectories from the 2dVar, IBI, OMA and 2dVar-opt fields during S1 (a) and S2 (b). Results are presented for drifter 8 of S1 and drifter 5 of S2. The travel distance is given in km at the end of each trajectory. The trajectory shown represents the typical behavior observed on all drifters during each survey. Zooms of (a) and (b) have been adjusted to provide the best representation of the trajectories.

During S1, the mean travel distance by drifters is 19.5 km. While OMA and IBI trajectories tend to give results close to observations, 2dVar and 2dVar-opt trajectories underestimate the travel distance. However, 2dVar-opt field respects the shape of the real trajectory (see Fig. 3a), which is not the case of 2dVar, OMA and IBI. During S2, the travel distance increased up to 61.6 km. Table 2 summarizes the results of the comparison of the different solutions used and shows that the 2dVar-opt field is the closest to observations. In contrast, IBI appears to underestimate the travel distance, while OMA and 2dVar tend to over-estimate it.

Regarding the *L* index and RMSE, the 2dVar field once again appears to be the most realistic compared to OMA and IBI fields. The *L* index of the 2dVar field is 31 % smaller than that of IBI, and 15 % smaller than that of the OMA field during S1. During S2, the *L* index of the 2dVar field is 23 % smaller than that of IBI and 11 % smaller than that of OMA. In terms of RMSE, the RMSE of 2dVar is 29 % smaller than that of IBI and 21 % smaller than that of OMA for S1. Similarly, for S2, it is 16 % smaller than that of IBI and 32 % smaller than that of OMA. This reinforces confidence in the 2dVar results. 2dVar-opt shows the lowest values of the index *L*, and RMSE, improving those of the 2dVar field. Regarding *L*, this reduction attains 30 % during S1 and 63 % during S2. Regarding the RMSE, the average decrease is 23 % during S1 and 35 % during S2.

When assessing the errors of the different surface velocity fields with time (Fig. 4) we observe that the 2dVar-opt field still appears to be the most realistic regarding the time series of the Lagrangian error index *L* (Fig. 4a, b) and the RMSE (Fig. 4c, d) as stated in Table 2. During S1, the Lagrangian error index of all the surface current fields peaked around 5 h, at the time where surface currents were low, and drifters were subject to tidal and inertial oscillations. The RMSE was also larger during the first few hours of deployment for all the surface current fields. During S2, there is no such peak found in *L* index and RMSE time series, surface drifters being advected by the coastal jet and not subject to tidal or in-ertial oscillation. However, during both surveys and regarding both L and RMSE, 2dVar and 2dVar-opt are systematically presenting the best performance compared to IBI and OMA.

With the aim of assessing the impact of the OI spatially in the area used for FLSE maps computation, Fig. 5 shows the difference in velocity resulting from the application of OI to the 2dVar fields corresponding to the period of surveys S1 and S2. First, during S1, the mean velocity field shows the presence of eddies in the study area, with low velocities and a coastal current oriented mainly along the Spanish coast. During S2, the mean 2dVar-opt velocity field presents larger velocities (see Table 2), mainly oriented alongshore. During both surveys, the largest difference values between the initial and optimized velocity fields are found in the coastal region 20–30 km large. During S1, the mean absolute difference is close to 0.05 m/s (Fig. 5a). 2dVar field is characterized by the mean

and maximum velocity of 0.08 m/s and 0.5 m/s respectively, while for 2dVar-opt the respective values are 0.1 m/s and 0.4 m/s (Table 2). Therefore, the OI of drifter velocities induced modifications in the remotely sensed velocity fields up to 20 %, on average. Because coastal circulation during S1 was characterized by low velocities, inertial and tidal oscillations, the major changes were obtained in the eastern and central parts of the study region, covered by drifter observations (Fig. 5a). In contrast, during S2, the mean absolute difference between initial and optimized fields is twice larger, 0.09 m/s. Larger differences, 0.15–0.20 m/s, are found in the nearshore region, extending up to 20 km offshore (Fig. 5b). However, significant modifications in the velocity filed (up to 0.1 m/s) observed at far ranges, ~40 km, demonstrate the global effect of drifter measurements near the shore on the velocity field within the whole study region.

For the 2dVar field, the mean and maximum surface current velocity are 0.2 m/s and 0.5 m/s, while in 2dvar-opt field they became respectively 0.3 m/s and 0.6 m/s (Table 2) indicating an increase of 45 %. The larger disparities observed during S2 can be related to higher current speed inside the current jet along the coast (Fig. 5b) occurring during this period of the year (Rubio et al., 2019).

Finally, as shown in Appendix C, the 2dVar-opt field proves to be the most accurate when compared to the absolute dispersion of virtual particles and to FSLE maps derived from alternative surface current fields. The results underline the accuracy of the 2dVar-opt field, which has the lowest Lagrangian and relative errors. Based on these results, the 2dVar-opt field will be used for further assessing CCS.

4.2. Absolute dispersion and CCS identification

Current velocity fields during the two survey periods revealed very different coastal dynamics largely influenced by the local wind and remote forcing.

S1 took place during a period of low winds with a mean speed of 3 m/s (Fig. 6a). During this period, surface currents were weak, and some drifter trajectories showed the influence of tidal motions and inertial oscillations (Fig. 6c). During S1, up to five local CCS were identified by the naked eye (not shown), in the form of rectilinear lines parallel to the coast in the area where the westernmost cluster of drifters was deployed. The local CCS observed closest to the coast (showcased in Fig. 2, and which determined the location of the third cluster of drifters) was the only one showing foam. However, macro litter aggregation was (quali-tatively) observed in several of them. The presence of CCS is also showcased in the Chl-a satellite images available during S1 survey dates (Fig. 6c). High values of Chl-a concentration are found close to the coast and associated with the presence of the main river plumes. The first alongshore line of high Chl-a values coincides with the CCS with foam
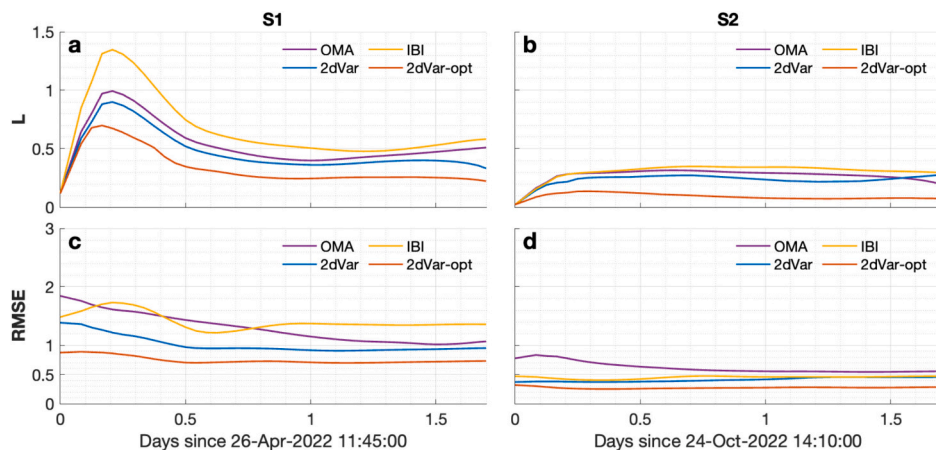

Fig. 4. *L* index (a, b) and RMSE (c, d) computed for the available fields. Figures related to S1 are given in the left column, while figures related to S2 are given in the right column.
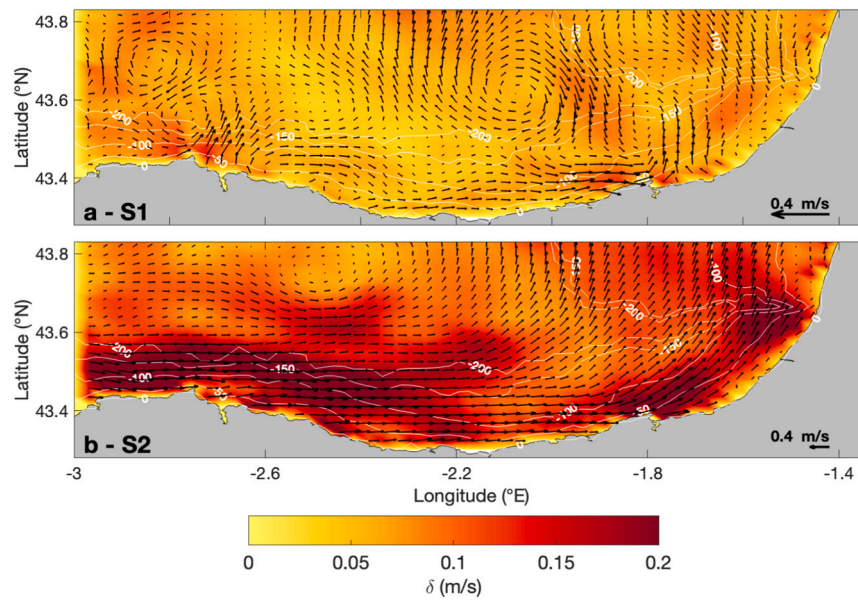
Fig. 5. Map of the differences induced by OI on the 2dVar fields. Red vectors represent the mean surface velocity from the 2dVar-opt field. Velocity scale is different for the two periods and is given by the reference arrow in the right bottom corner of each panel. Color shading shows the absolute averaged velocity differences $\delta = |\boldsymbol{u}_r - \boldsymbol{u}_{opt}|$ between 2dVar and 2dVar-opt fields over 40-h corresponding to the dates of S1 and S2 surveys, with the same color scale.

observed closest to the coast, and with the initial location of the drifters in the third cluster (Fig. 6c, −2.2°E; 43.3°N). This high Chl-a strip could result from the convergence of the plumes of the Deba, Urola and Oria rivers around −2.05°E; 43.33°N (Fig. 6c). Chl-a concentrations observed are above 1 mg.m-3. This particular area corresponds also to the zone of convergence of three drifters observed during S1, shown in red in Fig. 6c. Two pairs of drifters, initially separated by 8 and 16 km, were found separated by <2 km after a 40-h drift, which evidences convergence in the vicinity of the outer limit of the river plumes.

S2 took place under strong southwards winds, with a mean wind speed of 6 m/s (Fig. 6b). The current jet observed along the coast during this surveying period is at the origin of mostly rectilinear drifter trajectories (Fig. 6d). No CCS were identified during the survey, although (with much less extent than in S1) high Chl-a concentrations are found in the area around Deba and Urola rivers (where the drifters were deployed), and along the French coast. The S2 drifters did not encounter any visible local CCS along their drift, as observed in the Chl-a image for the corresponding date (Fig. 6d), at least until they arrived in the waters off the French coast, where the distribution of high Chl-a concentrations shows the Adour plume. No specific points of convergence for the drifters in S2 can be identified from the qualitative analysis of their trajectories (Fig. 6d).

To further investigate the influence of CCS on horizontal mixing, the absolute dispersion was computed based on analysis of real and virtual drifter trajectories (13 during S1, 9 during S2) reconstructed from 2dVar-opt fields. The absolute dispersion is computed along x- and y-axis directions (globally following the orientation of the coastline). First, the absolute dispersion computed from 2dVar-opt trajectories is consistent with observations regarding dispersion regimes, and dispersion rate in x and y directions. Nevertheless, an underestimation of the absolute dispersion by 37 %, during S1, and by 57 %, during S2, was found when 2dVar-opt trajectories were used, compared to that of real trajectories.

During the first 5 h of S1, the dispersion is nearly isotropic, with slightly larger alongshore dispersion, and the absolute dispersion follows a ballistic regime with $A^2(t) \sim t^2$ (Fig. 7a, c). Then, starting from 6 to 7 h, the dispersion becomes anisotropic with ten times larger dispersion in the alongshore direction (along x-axis). During this period of time, the absolute dispersion curve demonstrates equivalent to the diffusive dispersion regime with $A^2(t) \sim t$. This change in regime is due to the loss of correlation between the different trajectories as the real and virtual travel distances increase.

During S2, the dispersion is strongly anisotropic. The dispersion rate in the alongshore direction is found to be twelve times larger than in the cross-shore direction. The time evolution of absolute dispersion is found fundamentally different. For almost the entire period of S2, turbulent motions are characterized by ballistic regime with $A^2(t) \sim t^2$ (Fig. 7b, d). This dispersion regime is representative for powerful current systems such as the current observed along the coast.

During S1 and S2, high current velocities observed influence the distribution of CCS and suggest strong dynamics along the coast, compatible with the presence of alongshore CCS.

To characterize the spatial distribution of CCS, 24 hourly FSLE maps were generated from 2dVar-opt and averaged over one day corresponding to S1 and S2 surveys (Fig. 8a, b). The spatial distribution of large FSLE values, revealing the presence of intense horizontal stirring in the turbulent flow, were qualitatively compared with Chl-a concentrations for the same period (Fig. 8c, d for the same dates, and e, f for previous dates with better coverage).

During S1, the FSLE ridgelines, located at short distance from the shore, are aligned with the Spanish coast (Fig. 8, red square), supporting that surface current structuring is affected by a coastal downwelling. During S2, less FSLE ridgelines are found close to the Spanish coast, showing lower values. This is probably because at the surface, the current velocities were larger, leaving no time for particles to accumulate near the Spanish coast. During S2, CCS are mostly found parallel to the French coast (Fig. 8, red triangle). During both surveys, in the middle of the study area, further from the coast, the FSLE ridgelines are less organized and sometimes meandering.

From the examination of hourly FSLE maps during both S1 and S2, coastal CCS persist during the whole time of the surveys and slightly move in the dominant surface current direction, i.e. northeastward (not shown).

During S1, the coastal CCS, where three drifter trajectories converged (Fig. 6c, red trajectories), is shown in all panels of Fig. 8 by red square. This location corresponds to aLCS, which coincides with a Chl-a front and where a local CCS was identified to concentrate foam and macrolitter. FSLE ridgelines (red lines in Fig. 8) delimit the regions
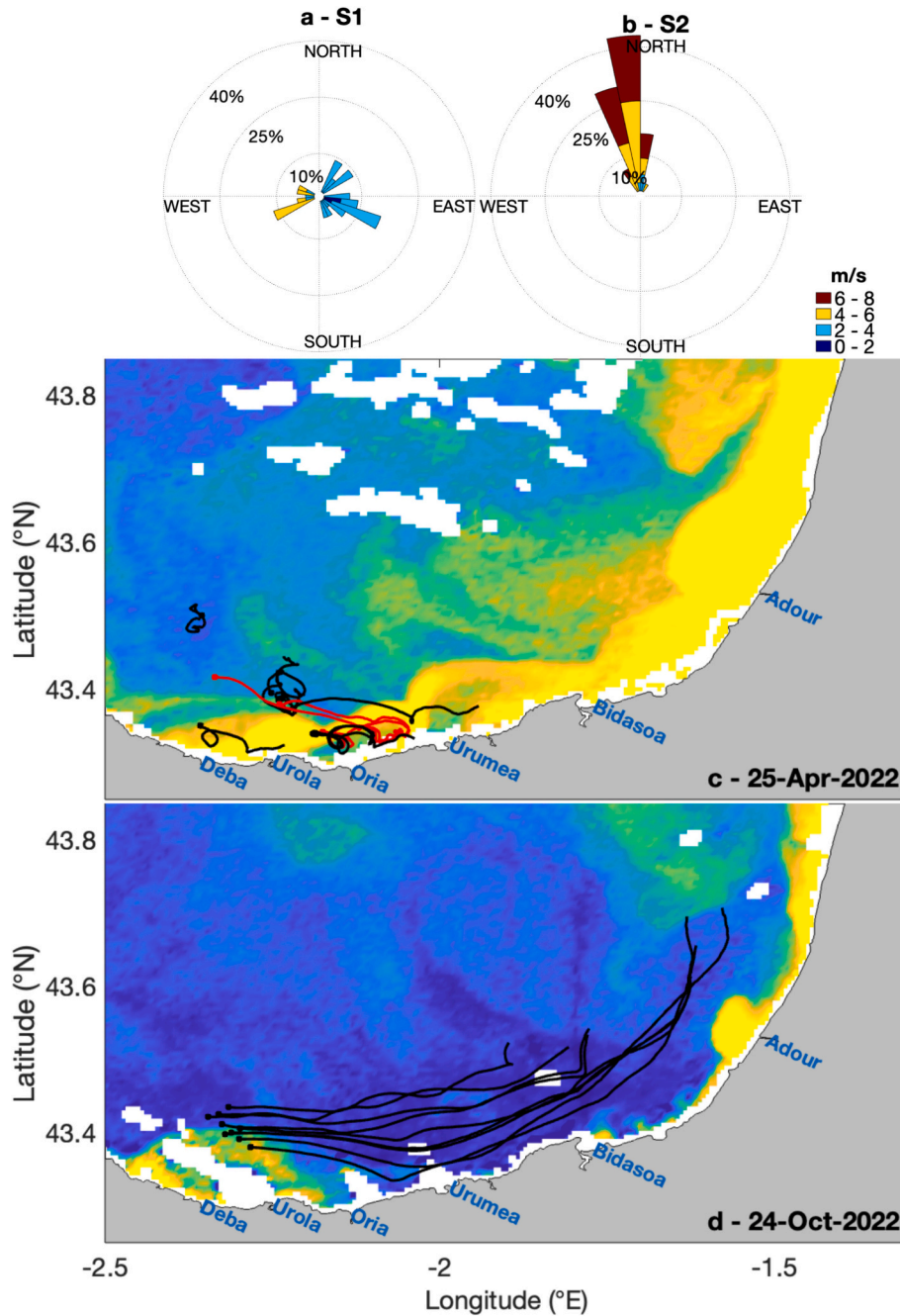
Fig. 6. Wind roses for (a) S1 and (b) S2 from the WFR model averaged over the S1 and S2 time periods and spatially-averaged over the study region. Trajectories of Lagrangian drifters released during (c) S1 and (d) S2 superimposed to the satellite Chl-a concentration from CMEMS at 300 m resolution on (c) April 25, 2022, and (d) October 24, 2022. Location of the main rivers is given by blue characters. The color bar is given in log scale. Drifter trajectories are shown in black, with a dot indicating the deployment location. The three drifters converging during S1 are shown in red in (c).
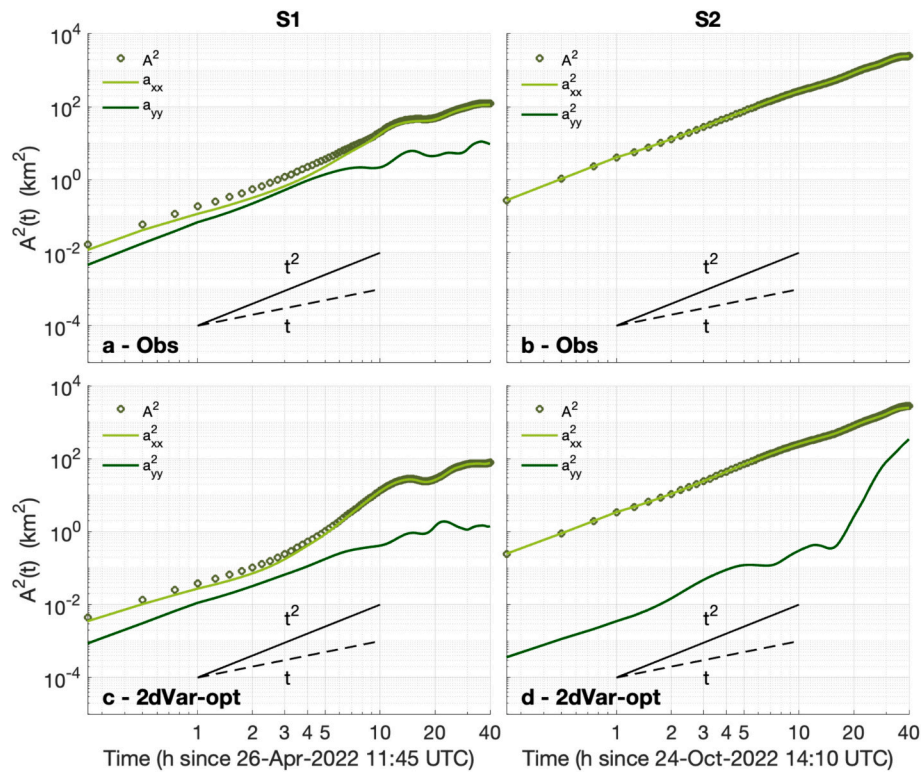
Fig. 7. Absolute dispersion considering observed drifter trajectories (a, b) and 2dVar-opt trajectories (c, d) during S1 and S2 surveys. The ballistic (t^2) and diffusive (t) regimes are shown by solid and dashed black lines, respectively.
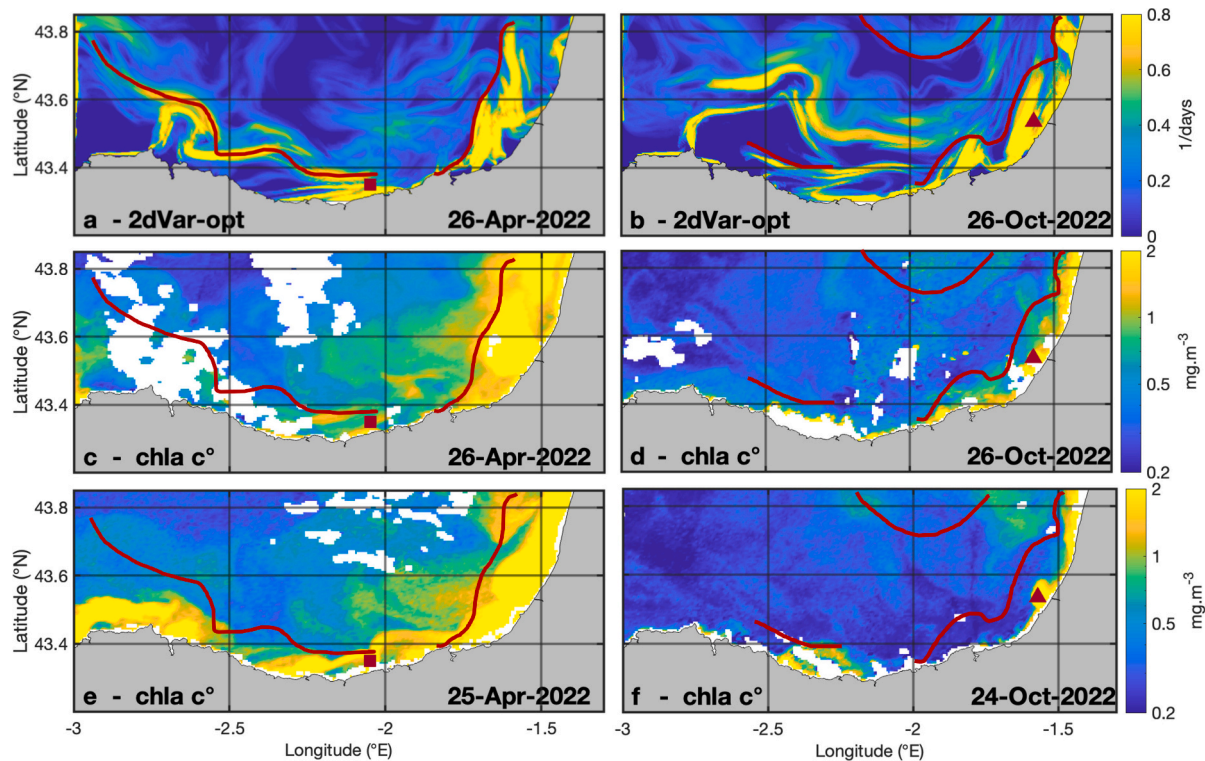
Fig. 8. FSLE maps averaged on April 26, 2022, and on October 26, 2022, computed from the 2dVar-opt field (a, b) respectively. Chl-a concentrations (c, d) derived from the 300 m resolution CMEMS product on (c) April 26, 2022, on (d) October 26, 2022, on (e) April 25, 2022, and on (f) October 24, 2022. Chl-a concentration is plotted in log scale. Specific locations mentioned in the text are shown with red squares and triangles and limits of some FSLE ridgelines are indicated by red lines.

of high Chl-a concentration, namely delineating the offshore limit of river plumes (ex. S1, red square) and in general of Regions of Freshwater Influence (ROFI). The eastern part of the FSLE maps and Chl-a concentration matches well on April 26, 2022. Nevertheless, due to the poor coverage of the image, the FSLE map was compared to another satellite image from the previous day, April 25, 2022. This second satellite image also matches the FSLE ridgelines, especially in the western part of the study area. The meander visible in FSLE ridgelines (Fig. 8a, −2.6°E, 43.6°N) delimits a region of high Chl-a, mostly visible on Fig. 8e.

During S2, comparisons between the FSLE map and Chl-a concentrations are more consistent with the satellite image of October 26, 2022 (Fig. 8d) than with another cloud-free image from two days earlier (Fig. 8f). The northernmost and easternmost FSLE ridgelines delimit regions of high Chl-a, mainly visible in the satellite image of the same day (Fig. 8d), whereas the satellite image of the previous two days shows lower Chl-a concentrations overall, except in the Adour plume (red triangle) and near the Spanish coast (−2.4°E, 43.3°N). The latter area is also delimited by the westernmost FSLE ridgeline, clearly visible in Fig. 8f. The location of the coastal jet (red triangle) shown in the FSLE map (Fig. 8b) is consistent with the high Chl-a concentration values visible in both satellite images (Fig. 8d, f).

5. Discussion

Improved identification of coastal CCS is achieved by mapping FSLE using a surface current field optimized by fusing HFR remote sensing data and surface drifter measurements, and completed by using satellite remote sensing data.

The efficiency of data assimilation schemes, based on OI of drifter velocity measurements in circulation models has been assessed in several studies (e.g. Belyaev et al., 2012; Molcard et al., 2003). Other techniques of surface current assimilation in circulation models, such as the Local Ensemble Transform Kalman Filter (Sun and Penny, 2019), 4DVar (Carrier et al., 2014; Muscarella et al., 2015), nudging and sequential methods (Isern-Fontanet et al., 2017), have also proven to be efficient. However, the approach proposed here, which involves merging velocity from HFR and drifter observations, is novel, easy to implement and requires minimal computational cost.

This approach can be applied in other coastal areas where surface velocity fields (from HFR observations or models) and surface drifter measurements are available. However, some adjustments may be necessary, particularly concerning the methods to obtain the covariance matrix used in the OI technique. These methods can be dependent on the targeted coastal area dynamics and the physical processes solved by the surface current available. For instance, in the southeastern BoB, a region with complex dynamics, including the inclusion of tides, inertial oscillation, and slope current was necessary to obtain accurate covariances. The same technique has been applied in the eastern English Channel (Bertin et al., 2024), a region mostly driven by tides, requiring fewer ensemble members to compose the OI covariance matrix due to the high correlation between ensemble members.

The good performance of the 2dVar method to retrieve accurate high-resolution gap-filled HFR velocity fields in the study area has been showcased for the targeted period. However, remote sensing of surface current velocity by HFR has limitations. The quality of HFR data can be affected by different issues related to hardware or software failures and unfavorable environmental conditions, like rough sea states, signal interference or modifications of the directional antenna patterns (Hernández-Carrasco et al., 2018b; Mantovani et al., 2020). This can compromise the availability of the data resulting in reduced range, incomplete spatial coverage or even periods without data. Moreover, the HFR baseline, the area between two radar sites in which the total currents cannot be reconstructed in an accurate way, is a permanent region of large uncertainty. The presence of spatio-temporal gaps prevents the use of the velocity data for Lagrangian analysis. So, the use of gap-filling methods is essential for the studying the transport and dispersion

processes in marine coastal environments. Even after application of gap-filling methods, the resulting velocity fields derived from HFR measurements are not free of errors (Hernández-Carrasco et al., 2018b). So, when an accurate description of small coastal features of coastal circulation is required, the use of an optimization method to reduce the impact of these errors is essential.

In this study, we first demonstrated the high performance of the 2dVar method for reconstructing the current velocity field. We also demonstrated that the OI of 2dVar fields provides the most realistic picture of surface current velocities, and therefore of the location of CCS in the study area. The shape, location and dimensions of these structures vary significantly with time, at seasonal scales, as shown by the comparison between the two surveys, and at shorter scales. It is therefore crucial to correctly characterize the CCS because of their role in the aggregation of marine litter and other materials such as particulate materials or pollutants (Cózar et al., 2021; Ruiz et al., 2020). The Lagrangian assessment of the coastal dynamics enables locating such CCS through the computation of FSLE, since their ridgelines indicate the location of converging Lagrangian trajectories (Hernández-Carrasco et al., 2018a). A notable advantage of FSLE is their ability to unveil oceanic structures at a finer scale than the nominal resolution of the velocity field under analysis, as demonstrated by Hernández-Carrasco et al. (2011). This allows FSLE to capture sub-mesoscale processes more effectively, and the results offer an accurate representation of oceanic transport properties.

FSLE ridgelines, obtained using the optimized velocity fields, were found mainly aligned with the coastline. The coastal CCS depicted scales ranging from 10 to 50 km in the alongshore direction and were much more intense closer to the coast. During S1, the presence of intense or persistent structures was concentrated mostly over the shelf, within a strip of 20 km from the coast, while during S2, CCS were also present in off shelf waters. Large horizontal stirring of real and virtual drifters in the alongshore direction is also supported by the anisotropic character of the absolute dispersion at the end of S1 and during the whole duration of S2. During these periods of time, the zonal component of the absolute dispersion is dominant, in good agreement with CCS orientation parallel to the Spanish Basque coast. Similar situation was observed along the French coast, where FSLE ridgelines were also aligned with the coastline. In both cases, FSLE ridgelines showed a strong alignment with the patterns of high Chl-a concentration and indicated the offshore limit of river plumes, or, more generally, ROFIs.

The comparison performed between FSLE maps and Chl-a spatial distribution is qualitative. First, the remote sensing of Chl-a concentration in coastal waters may still lack reliability and depends on the accuracy of the atmospheric correction, the Chl-a concentration retrieval models and the scale effects of these retrieval models (Chen et al., 2013). Second, to use Chl-a as a passive tracer is especially challenging in coastal areas, where nearshore biogeochemical processes are known to modulate Chl-a concentrations. A possibility to enable quantitative comparisons will be to decompose the Chl-a time series data (with an empirical orthogonal function method or a frequency analysis) into its different components, isolating the more conservative part of the signal. This approach required continuous time series of daily Chl-a concentration (Alvera-Azcárate et al., 2009; Beckers et al., 2006), which were not available during S1 and S2 due to the presence of clouds.

However, satellite ocean color products appear used for investigating the link between coastal CCS and the spatial distribution of particulate material. At larger scales, d'Ovidio et al. (2010, 2015) and Hernández-Carrasco et al. (2018a), demonstrated that FSLE ridgelines were found to act as dynamic barriers, exerting a significant influence on the structuring of the Chl-a field. Ridgelines delimit the Chl-a distribution in space and highlight the crucial role played by small-scale coastal hydrodynamics in shaping the intricate patterns observed in the Chl-a concentrations. During S1 survey, the FSLE ridgeline nearest to the Spanish coast aligned with elevated concentrations of Chl-a, primarily linked to the runoff of the Deba, Urola, and Oria rivers. This convergence

zone also corresponded to the area where drifters' trajectories tended to converge, and where noticeable quantitative concentrations of macro litter and foam were observed in surface waters. The observed CCS and aggregation of macro litter items observed during S1 survey are consistent with previous observations in the area made by (Ruiz et al., 2020). Further research is needed to study the occurrence, loads and fate of litter aggregating in CCS.

The CCS mapping and optimization methods developed here can be applied to operational data for different applications and in situations of vulnerability. For example, in the case of massive waste arrivals in certain areas or oil spill, or for applications such as fishing or search and rescue at sea, where CCS can be used as an indicator of high concentration of fishing resources or areas where search efforts could be intensified. This work can also be combined with satellite imagery data (Rußwurm et al., 2023; Cózar et al., 2024) to provide operational information on marine litter aggregation in coastal areas.

6. Conclusions

A method of efficient identification of coastal CCS in the southeastern BoB is proposed in this study. The findings demonstrated, first, that the surface current field obtained from the 2dVar interpolation of radial HFR velocities provided the best performance compared to the other Eulerian fields, commonly used in the community, like HFR-based OMA product, and modeled fields (IBI). The best performance of 2dVar was observed regarding the Lagrangian error and RMSE obtained from real and virtual trajectories and regarding the identification of CCS. Then, the fusion of 2dVar surface current fields and drifter velocity measurements by means of OI further decreased the Lagrangian error index by 50 % and reduced the RMSE by 30 %. Notably, the optimized 2dVar field (2dVar-opt) was found to provide the most realistic location of CCS. We demonstrated the presence of intense horizontal stirring in the turbulent flow close to the Spanish and French coasts leading to the formation of coastal CCS, aggregating particulate matter. By using the Lagrangian approach, and more specifically FSLE estimation and mapping, we were able to determine the location of the CCS more accurately and we demonstrated that FSLE ridgelines delimit the spatial distribution Chl-a.

These results represent a significant advance in the identification of CCS from remotely sensed surface current velocity and have direct applications for the study of marine litter transport and aggregation. This knowledge is essential in physical oceanography because marine litter serve as tracers for comprehending sub-mesoscale ocean circulation. Inversely, our comprehension of ocean currents plays a significant role in determining floating marine litter pathways. This, in turn, facilitates research and pollution mitigation, which is particularly important in a coastal-dependent society.

The distribution and extension of CCS at subsurface layers and how these structures can affect the transport of floating marine debris of different buoyancy remains unknown. Future research will be focused on studying the vertical dimension of CCS by using 3D model outputs. Another interesting aspect will be to study the impact of different wind drag coefficients in the Lagrangian computations of trajectories and FSLEs in this area. This aspect may be relevant for floating marine debris with sections directly exposed to the wind. Understanding how the wind will influence the CCS spatial distribution and the transport and accumulation of floating marine debris of different nature could provide

significant information for more accurate simulations.

CRediT authorship contribution statement

S. Bertin: Writing – original draft, Visualization, Software, Resources, Project administration, Methodology, Investigation, Formal analysis, Data curation. **A. Rubio:** Writing – review & editing, Validation, Supervision, Resources, Project administration, Methodology, Investigation, Funding acquisition, Conceptualization. **I. Hernández-Carrasco** Writing – review & editing, Software, Methodology. **L. Solabarrieta:** Writing – review & editing, Software, Methodology. **I. Ruiz:** Writing – review & editing, Methodology, Investigation. **A. Orfila:** Writing – review & editing, Software, Methodology. **A. Sentchev:** Writing – review & editing, Validation, Supervision, Methodology, Investigation, Funding acquisition, Conceptualization.

Declaration of competing interest

The authors declare that they have no known competing financial interests or personal relationships that could have appeared to influence the work reported in this paper.

Data availability

Data will be made available on request.
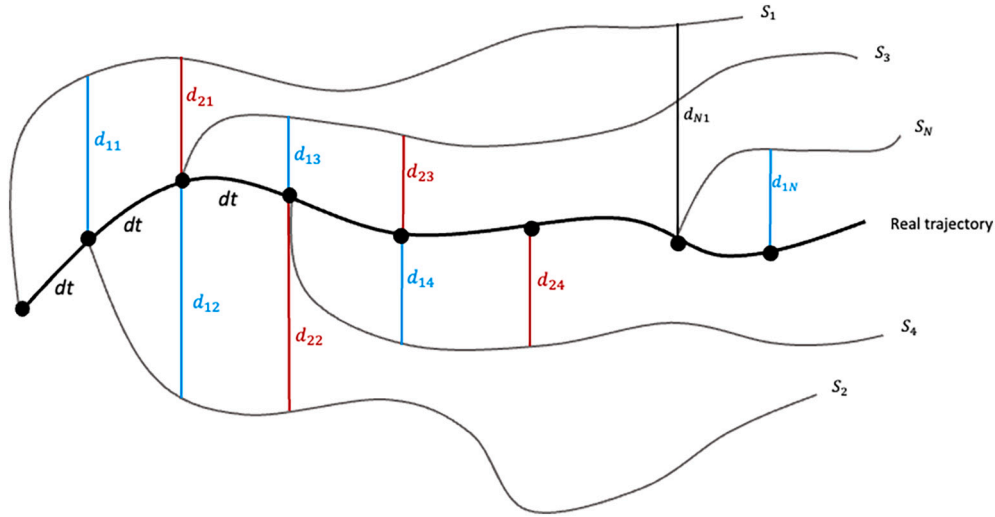
Appendix A. Computation of the Lagrangian error

Fig. A. Schematic of the computation of the Lagrangian error for one drifter. The real drifter trajectory corresponds to the black line, and the *N* virtual trajectories deployed every *dt* (*dt = 1* h*)* corresponds to the grey lines.

Based on Fig. A, the steps of computation of the Lagrangian error are the following:

$$D_1 = D(1dt) = \frac{d_{11} + d_{12} + d_{13} + \ldots + d_{1N}}{N}$$

$$D_2 = D(2dt) = \frac{d_{21} + d_{22} + d_{23} + \ldots + d_{2N-1}}{N-1}$$

$$D_3 = D(3dt) = \frac{d_{31} + d_{32} + d_{33} + \ldots + d_{2N-2}}{N-2}$$

$$\ldots$$

$$D_{N-1} = D((N-1)dt) = \frac{d_{(N-1)1} + d_{(N-1)2}}{2}$$

$$D_N = D(Ndt) = d_{N1}$$

Appendix B. Sensitivity test to the number of clusters in K-Means and to the number of ensemble members in OI covariance matrix

As described in Chapter 3.6, the non-linear K-Means clustering algorithm was utilized for two main objectives. These objectives included identifying dominant surface current groups during each survey and extracting ensemble members that shared similar dominant groups as observed during each survey period, accounting for 90 % of the variability. In order to identify the optimal number of clusters for each survey, we conducted experiments involving varying cluster counts within the K-Means method (refer to Table B1).

It was decided that 8 and 6 clusters of one hour each were sufficient to represent around 40 h of survey time (Table B1, grey shaded lines), and the sensitivity test was continued by taking 35 and 12 clusters in the K-Means method. Simultaneously to the sensitivity test for the number of clusters in the K-Means method, we also conducted a sensitivity test for the number of ensemble members comprising the OI covariance matrix. To construct this covariance matrix, we first identified the predominant groups observed during each survey. Subsequently, we extracted ensemble members that exhibited the same predominant groups in a similar order of magnitude from the year-long 2dVar field (covering January 2022 to December 2022), which included data from both surveys. It is important to notice that every chosen ensemble member aligned with the same tidal stage as the survey in question. To prevent any tidal influence, we exclusively opted for ensemble members synchronized with the tidal oscillations, even though tides contribute to a relatively small portion of the total kinetic energy in the study area (approximately 10 to 15 %, as indicated by Solabarrieta et al., 2014).

Table B1
Number of representative clusters found during S1 and S2 using different number of K-Means clusters, with 90 % of variability explained. Grey shaded lines correspond to the number of K-Means clusters we decided to further test.

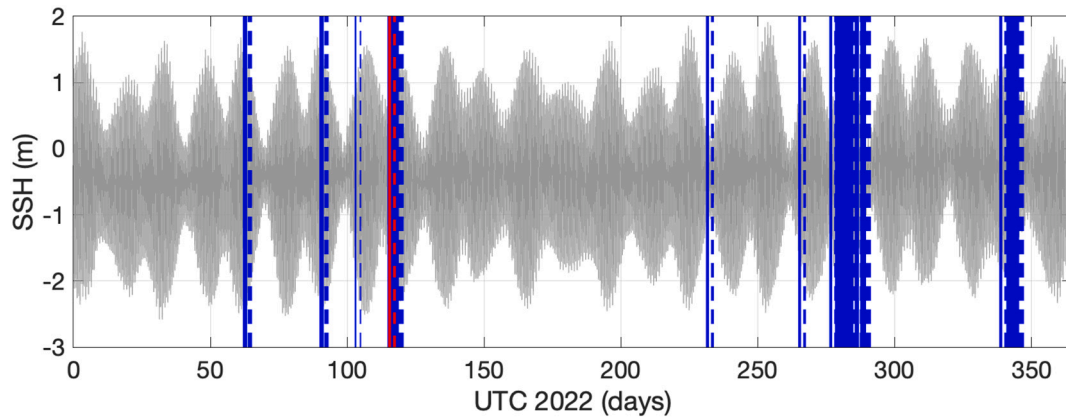| Variability explained (%)	Number of clusters	Number of clusters in S1	Number of clusters in S2
90	50	10	9
	45	9	10
	35	8	8
	25	6	7
	12	6	5

Fig. B1. An example of 80 ensemble members (in blue) extracted from the 1-year long 2dVar field. S1 period is shown in red. Sea surface height (SSH) from IBI model run is given in grey.

Subsequently, we calculated the RMSE (Table B2) and the Lagrangian errors (Table B3) for both the initial 2dVar field and the optimized 2dVar field, with the covariance matrix comprising 20, 40, 60, and 80 ensemble members. Notably, Tables B2 and B3 underscore that the outcomes of the OI technique are notably influenced by the number of ensemble members used in the OI covariance matrix, rather than the number of clusters employed in the K-Means clustering method. Across 35 and 12 K-Means clusters, transitioning from 20 to 80 ensemble members in the OI covariance matrix yielded a 12 % reduction in RMSE during S1 and a 17 % reduction during S2 (as indicated in Table B2). Conversely, opting for 35 K-Means clusters instead of 12 only marginally decreased the Lagrangian error (averaged over the number of ensemble members in the OI covariance matrix) by 1.6 % during S1 and 4.6 % during S2. Regarding the Lagrangian error, averaged over 35 and 12 K-Means clusters, increasing the number of ensemble members in the OI covariance matrix from 20 to 80 resulted in a 10 % decrease in error during S1 and a substantial 40 % reduction during S2 (as detailed in Table B3). In contrast, choosing 35 K-Means clusters over 12 led to a modest reduction of the Lagrangian error index by 1 % during S1 and 9 % during S2. It is not surprising that the OI outcomes were particularly responsive to the number of ensemble members comprising the covariance matrix, given the intricate dynamics prevalent in the southeastern BoB. This region exhibits a complex interplay of various influences, including freshwater inputs, swell, inertial oscillations, and tides.

Table B2
Mean RMSE computed from Eq. 3 for both surveys considering 35 and 12 K-Means clusters and a number of ensemble members varying from 20 to 80. The mean error was computed from the initial 2dVar field (column 3) and the optimized 2dVar field (column 5). The standard deviation of the mean error of the optimized field is given at the 5th column.

	Number of clusters K-Means	Number of ensemble members OI	$RMSE_r$	$RMSE_{opt}$
S1	35	20	0.94	0.80
		40		0.77
		60		0.75
		80		0.73
	12	20		0.81
		40		0.79
		60		0.72
		80		0.72
S2	35	20	0.43	0.32
		40		0.30
		60		0.29
		80		0.28
	12	20		0.34
		40		0.31
		60		0.29
		80		0.28

Therefore, in the sensitivity test regarding the number of K-Means clusters, we opted for 12 clusters, as it yields nearly identical results to using 35 clusters, with the added advantages of reducing computational costs and aligning with the findings of (Solabarrieta et al., 2015), who demonstrated that 12 K-Means clusters were adequate for assessing variability in the southeastern BoB.

Hence, regarding the sensitivity test to the number of K-Means clusters, we chose to employ 12 as it is giving approximately the same results as 35 for practical reasons: it reduced the computational cost, and it was proven that 12 K-Means clusters were sufficient to assess for the variability in the southeastern BoB. The 12 clusters are shown in Fig. B2. In the sensitivity analysis regarding the number of ensemble members forming the OI covariance matrix, the study's results were derived using 80 ensemble members, as it consistently produced the most favorable outcomes in both survey periods.

Table B3
Mean Lagrangian error index *L* computed for both surveys considering 35 and 12 K-Means clusters and a number of ensemble members varying from 20 to 80.

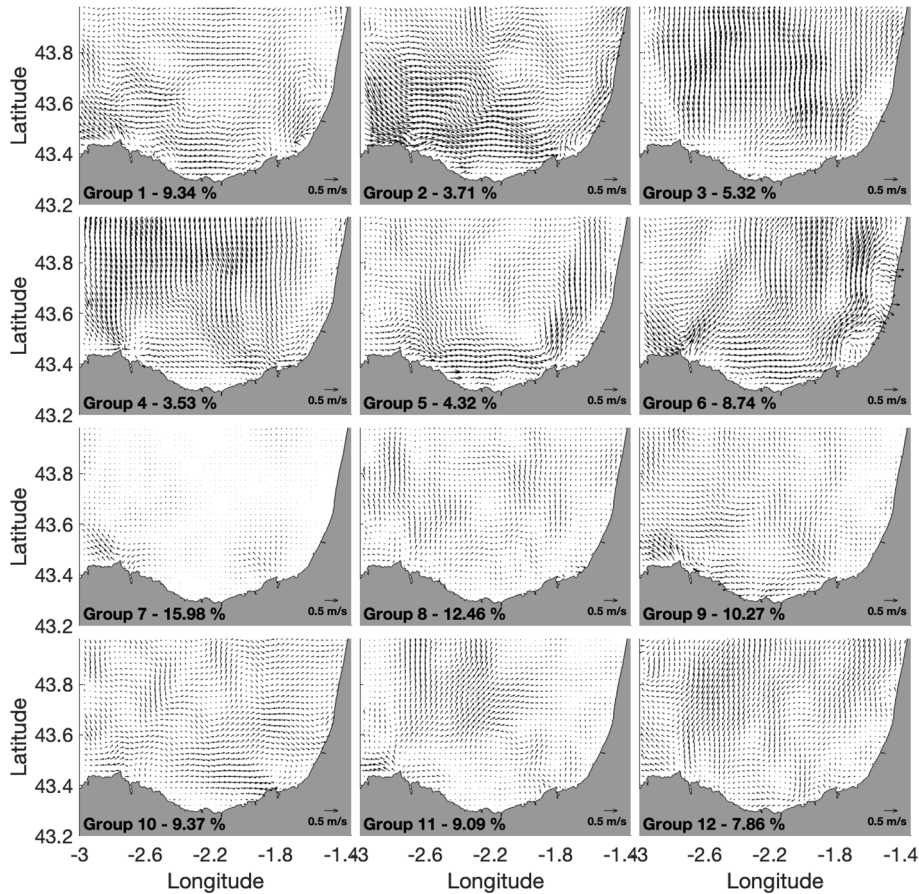|	Number of clusters K-Means	Number of OI ensemble members	L_r	L_{opt}
S1	35	20	0.5	0.37
		40		0.36
		60		0.35
		80		0.32
	12	20		0.37
		40		0.35
		60		0.36
		80		0.32
S2	35	20	0.2	0.13
		40		0.10
		60		0.09
		80		0.10
	12	20		0.15
		40		0.10
		60		0.10
		80		0.09

Fig. B2. 4 × 3 lattice of the K-Means algorithm applied to HFR surface currents from January 2020 to December 2022. The percentage of variability explained by each group is given in the title.

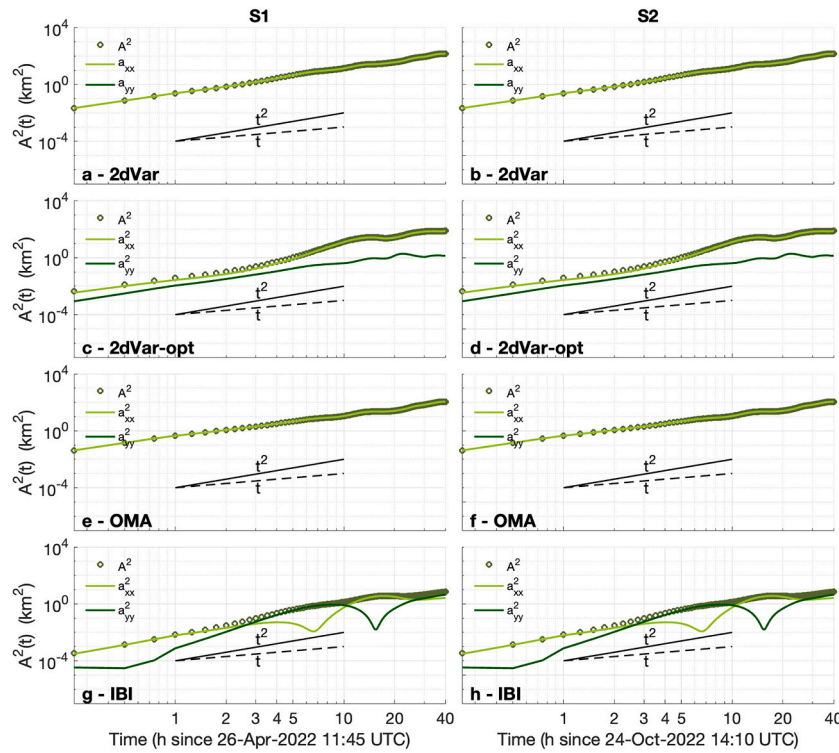## Appendix C. Lagrangian metrics of the different surface current fields

Fig. C1. Absolute dispersion along x and y computed from Eq. (4) for the modeled trajectories using 2dVar, 2dVar optimized, OMA and IBI surface current fields during S1 (left column) and S2 (right column). The ballistic (t^2) and diffusive (t) laws are shown by the black line and dashed black line respectively.
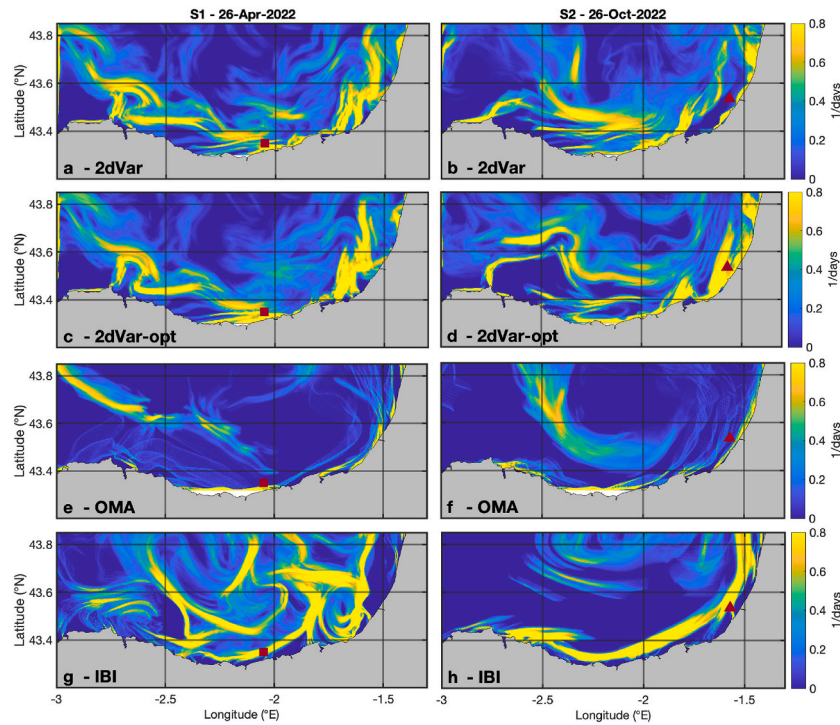

Fig. C2. FSLE maps averaged on the 26th of April 2022 (left column) and on the 26th of October 2022 (right column) computed from the initial 2dVar field (a, b), the optimized 2dVar field (c, d), OMA field (e, f) and IBI field (g, h). Specific locations mentioned in the text are shown with red square and triangle symbols.

References

Alvera-Azcárate, A., Barth, A., Sirjacobs, D., Beckers, J.-M., 2009. Enhancing temporal correlations in EOF expansions for the reconstruction of missing data using DINEOF. Ocean Sci. 5, 475–485. https://doi.org/10.5194/os-5-475-2009.

Aurell, E., Boffetta, G., Crisanti, A., Paladin, G., Vulpiani, A., 1997. Predictability in the large: an extension of the concept of Lyapunov exponent. J. Phys. A Math. Gen. 30, 1. https://doi.org/10.1088/0305-4470/30/1/003.

Ayouche, A., Carton, X., Charria, G., Theettens, S., Ayoub, N., 2020. Instabilities and vertical mixing in river plumes: application to the Bay of Biscay. Geophysical & Astrophysical Fluid Dynamics 114, 650–689. https://doi.org/10.1080/03091929.2020.1814275.

Basurko, O.C., Ruiz, I., Rubio, A., Beldarrain, B., Kukul, D., Cózar, A., et al., 2022. The coastal waters of the south-East Bay of Biscay a dead-end for neustonic plastics. Mar. Pollut. Bull. 181, 113881 https://doi.org/10.1016/j.marpolbul.2022.113881.

Beckers, J.-M., Barth, A., Alvera-Azcárate, A., 2006. DINEOF reconstruction of clouded images including error maps – application to the Sea-Surface Temperature around Corsican Island. Ocean Sci. 2, 183–199. https://doi.org/10.5194/os-2-183-2006.

Belkin, I.M., O'Reilly, J.E., 2009. An algorithm for oceanic front detection in chlorophyll and SST satellite imagery. Journal of Marine Systems, Special Issue on Observational Studies of Oceanic Fronts 78, 319–326. https://doi.org/10.1016/j.jmarsys.2008.11.018.

Belyaev, K.P., Tanajura, C.A.S., Tuchkova, N.P., 2012. Comparison of methods for argo drifters data assimilation into a hydrodynamical model of the ocean. Oceanology 52, 593–603. https://doi.org/10.1134/S0001437012050025.

Berline, L., Zakardjian, B., Molcard, A., Ourmières, Y., Guihou, K., 2013. Modeling jellyfish Pelagia noctiluca transport and stranding in the Ligurian Sea. Mar. Pollut. Bull. 70, 90–99. https://doi.org/10.1016/j.marpolbul.2013.02.016.

Berti, S., Alves Dos Santos, F., Lacorata, G., Vulpiani, A., 2011. Lagrangian drifter dispersion in the Southwestern Atlantic Ocean. J. Phys. Oceanogr. 41, 1659–1672. https://doi.org/10.1175/2011JPO4541.1.

Bertin, S., Sentchev, A., Alekseenko, E., 2024. Fusion of Lagrangian drifter data and numerical model outputs for improved assessment of turbulent dispersion. EGUsphere 1–24. https://doi.org/10.5194/egusphere-2024-176 [preprint].

Borja, A., Amouroux, D., Anschutz, P., Gómez-Gesteira, M., Uyarra, M.C., Valdés, L., 2019. Chapter 5 - the Bay of Biscay. In: Sheppard, C. (Ed.), World Seas: An Environmental Evaluation, Second edition. Academic Press, pp. 113–152. https://doi.org/10.1016/B978-0-12-805068-2.00006-1.

Bouzaiene, M., Menna, M., Poulain, P.-M., Bussani, A., Elhmaidi, D., 2020. Analysis of the surface dispersion in the Mediterranean sub-basins. Front. Mar. Sci. 7.

Budyansky, M.V., Goryachev, V.A., Kaplunenko, D.D., Lobanov, V.B., Prants, S.V., Sergeev, A.F., Shlyk, N.V., Uleysky, M.Yu., 2015. Role of mesoscale eddies in transport of Fukushima-derived cesium isotopes in the ocean. Deep-Sea Res. I Oceanogr. Res. Pap. 96, 15–27. https://doi.org/10.1016/j.dsr.2014.09.007.

Carrier, M.J., Ngodock, H., Smith, S., Jacobs, G., Muscarella, P., Ozgokmen, T., Haus, B., Lipphardt, B., 2014. Impact of assimilating ocean velocity observations inferred from Lagrangian drifter data using the NCOM-4DVAR. Mon. Weather Rev. 142, 1509–1524. https://doi.org/10.1175/MWR-D-13-00236.1.

Chapman, C.C., Lea, M.-A., Meyer, A., Sallée, J.-B., Hindell, M., 2020. Defining Southern Ocean fronts and their influence on biological and physical processes in a changing climate. Nat. Clim. Chang. 10, 209–219. https://doi.org/10.1038/s41558-020-0705-4.

Charria, G., Lazure, P., Le Cann, B., Serpette, A., Reverdin, G., Louazel, S., Batifoulier, F., Dumas, F., Pichon, A., Morel, Y., 2013. Surface layer circulation derived from Lagrangian drifters in the Bay of Biscay. Journal of Marine Systems, XII International Symposium on Oceanography of the Bay of Biscay 109–110, S60–S76. https://doi.org/10.1016/j.jmarsys.2011.09.015.

Chen, J., Zhang, M., Cui, T., Wen, Z., 2013. A review of some important technical problems in respect of satellite remote sensing of chlorophyll-a concentration in coastal waters. Selected Topics in Applied Earth Observations and Remote Sensing, IEEE Journal of 6, 2275–2289. https://doi.org/10.1109/JSTARS.2013.2242845.

Chenillat, F., Huck, T., Maes, C., Grima, N., Blanke, B., 2021. Fate of floating plastic debris released along the coasts in a global ocean model. Mar. Pollut. Bull. 165 https://doi.org/10.1016/j.marpolbul.2021.112116.

Cózar, A., Echevarría, F., González-Gordillo, J.I., Irigoien, X., Úbeda, B., Hernández-León, S., Palma, Á.T., Navarro, S., García-de-Lomas, J., Ruiz, A., Fernández-de-Puelles, M.L., Duarte, C.M., 2014. Plastic debris in the open ocean. Proc. Natl. Acad. Sci. 111, 10239–10244. https://doi.org/10.1073/pnas.1314705111.

Cózar, A., Aliani, S., Basurko, O.C., Arias, M., Isobe, A., Topouzelis, K., Rubio, A., Morales-Caselles, C., 2021. Marine litter windrows: a strategic target to understand and manage the ocean plastic pollution. Front. Mar. Sci. 8.

Cózar, A., Arias, M., Suaria, G., et al., 2024. Proof of concept for a new sensor to monitor marine litter from space. Nat. Commun. 15, 4637. https://doi.org/10.1038/s41467-024-48674-7.

Dagestad, K.-F., Röhrs, J., Breivik, Ø., Ådlandsvik, B., 2018. OpenDrift v1.0: a generic framework for trajectory modelling. Geosci. Model Dev. 11, 1405–1420. https://doi.org/10.5194/gmd-11-1405-2018.

D'Asaro, E., Shcherbina, A., Klymak, J., Molemaker, J., Novelli, G., Guigand, C., Haza, A., Haus, B., Ryan, E., Jacobs, G., Huntley, H., Laxague, N., Chen, S., Judt, F., McWilliams, J., Barkan, R., Kirwan, A., Poje, A., Özgökmen, T., 2018. Ocean convergence and the dispersion of flotsam. Proc. Natl. Acad. Sci. 115, 201718453 https://doi.org/10.1073/pnas.1718453115.

Davila, X., Rubio, A., Artigas, L.F., Puillat, I., Manso-Narvarte, I., Lazure, P., Caballero, A., 2021. Coastal submesoscale processes and their effect on phytoplankton distribution in the southeastern Bay of Biscay. Ocean Sci. 17, 849–870. https://doi.org/10.5194/os-17-849-2021.

Davis, R.E., 1983. Oceanic property transport, Lagrangian particle statistics, and their prediction. J. Mar. Res. 41, 163–194.

Declerck, A., Delpey, M., Rubio, A., Ferrer, L., Basurko, O.C., Mader, J., Louzao, M., 2019. Transport of floating marine litter in the coastal area of the south-eastern Bay of Biscay: a Lagrangian approach using modelling and observations. Journal of Operational Oceanography 12, S111–S125. https://doi.org/10.1080/1755876X.2019.1611708.

Della Penna, A., Koubbi, P., Cotté, C., Bon, C., Bost, C.-A., d'Ovidio, F., 2017. Lagrangian Analysis of Multi-satellite Data in Support of Open Ocean Marine Protected Area Design. Deep Sea Research Part II: Topical Studies in Oceanography, Future of Oceanic Animals in a Changing Ocean, 140, pp. 212–221. https://doi.org/10.1016/j.dsr2.2016.12.014.

d'Ovidio, F., Fernández, V., Hernández-García, E., López, C., 2004. Mixing structures in the Mediterranean Sea from finite-size Lyapunov exponents. Geophys. Res. Lett. 31 https://doi.org/10.1029/2004GL020328.

d'Ovidio, F., De Monte, S., Alvain, S., Dandonneau, Y., Lévy, M., 2010. Fluid dynamical niches of phytoplankton types. Proc. Natl. Acad. Sci. 107, 18366–18370. https://doi.org/10.1073/pnas.1004620107.

d'Ovidio, F., Della Penna, A., Trull, T.W., Nencioli, F., Pujol, M.-I., Rio, M.-H., Park, Y.-H., Cotté, C., Zhou, M., Blain, S., 2015. The biogeochemical structuring role of horizontal stirring: Lagrangian perspectives on iron delivery downstream of the Kerguelen Plateau. Biogeosciences 12, 5567–5581. https://doi.org/10.5194/bg-12-5567-2015.

Egbert, G.D., Erofeeva, S.Y., 2002. Efficient inverse modeling of barotropic ocean tides. J. Atmos. Ocean. Technol. 19, 183–204. https://doi.org/10.1175/1520-0426(2002)019<0183:EIMOBO>2.0.CO;2.

Enrile, F., Besio, G., Stocchino, A., Magaldi, M.G., 2019. Influence of initial conditions on absolute and relative dispersion in semi-enclosed basins. PLoS One 14, e0217073. https://doi.org/10.1371/journal.pone.0217073.

Ferrer, L., Fontán, A., Mader, J., Chust, G., González, M., Valencia, V., Uriarte, A.D., Collins, M.B., 2009. Low-salinity Plumes in the Oceanic Region of the Basque Country. Continental Shelf Research, 100 Years of Research within the Bay of Biscay, 29, pp. 970–984. https://doi.org/10.1016/j.csr.2008.12.014.

Ghosh, A., Suara, K., McCue, S.W., Yu, Y., Soomere, T., Brown, R.J., 2021. Persistency of debris accumulation in tidal estuaries using Lagrangian coherent structures. Sci. Total Environ. 781, 146808 https://doi.org/10.1016/j.scitotenv.2021.146808.

González, M., Uriarte, A., Fontán, A., Mader, J., Gyssels, P., 2004. Oceanography. Marine environment. Basque country. In: Marine Dynamics, pp. 133–157.

Gove, J.M., Whitney, J.L., McManus, M.A., Lecky, J., Carvalho, F.C., Lynch, J.M., Li, J., Neubauer, P., Smith, K.A., Phipps, J.E., Kobayashi, D.R., Balagso, K.B., Contreras, E. A., Manuel, M.E., Merrifield, M.A., Polovina, J.J., Asner, G.P., Maynard, J.A., Williams, G.J., 2019. Prey-size plastics are invading larval fish nurseries. Proc. Natl. Acad. Sci. 116, 24143–24149. https://doi.org/10.1073/pnas.1907496116.

Hastie, T., Tibshirani, R., Friedman, J., 2009. Prototype methods and nearest-neighbors. In: Hastie, T., Tibshirani, R., Friedman, J. (Eds.), The Elements of Statistical Learning: Data Mining, Inference, and Prediction, Springer Series in Statistics. Springer, New York, NY, pp. 459–483.

Hernández-Carrasco, I., López, C., Hernández-García, E., Turiel, A., 2011. How reliable are finite-size Lyapunov exponents for the assessment of ocean dynamics? Ocean Model 36, 208–218. https://doi.org/10.1016/j.ocemod.2010.12.006.

Hernández-Carrasco, I., Orfila, A., Rossi, V., Garçon, V., 2018a. Effect of small scale transport processes on phytoplankton distribution in coastal seas. Sci. Rep. 8, 8613. https://doi.org/10.1038/s41598-018-26857-9.

Hernández-Carrasco, I., Solabarrieta, L., Rubio, A., Esnaola, G., Reyes, E., Orfila, A., 2018b. Impact of HF radar current gap-filling methodologies on the Lagrangian assessment of coastal dynamics. Ocean Sci. 14, 827–847. https://doi.org/10.5194/os-14-827-2018.

Huntley, H.S., Lipphardt Jr., B.L., Jacobs, G., Kirwan Jr., A.D., 2015. Clusters, deformation, and dilation: diagnostics for material accumulation regions. J. Geophys. Res. Oceans 120, 6622–6636. https://doi.org/10.1002/2015JC011036.

Isern-Fontanet, J., Ballabrera-Poy, J., Turiel, A., García-Ladona, E., 2017. Remote sensing of ocean surface currents: a review of what is being observed and what is being assimilated. Nonlinear Process. Geophys. 24, 613–643. https://doi.org/10.5194/npg-24-613-2017.

Johnson, D.R., Perry, H.M., Graham, W.M., 2005. Using nowcast model currents to explore transport of non-indigenous jellyfish in the Gulf of Mexico. Mar. Ecol. Prog. Ser. 305, 139–146. https://doi.org/10.3354/meps305139.

Jones, C.E., Dagestad, K.-F., Breivik, Ø., Holt, B., Röhrs, J., Christensen, K.H., Espeseth, M., Brekke, C., Skrunes, S., 2016. Measurement and modeling of oil slick transport. J. Geophys. Res. Oceans 121, 7759–7775. https://doi.org/10.1002/2016JC012113.

Kaplan, D.M., Lekien, F., 2007. Spatial interpolation and filtering of surface current data based on open-boundary modal analysis. J. Geophys. Res. Oceans 112. https://doi.org/10.1029/2006JC003984.

Kershaw, P.J., 2016. Marine Plastic Debris and Microplastics–Global Lessons and Research to Inspire Action and Guide Policy Change.

LaCasce, J.H., 2008. Statistics from Lagrangian observations. Prog. Oceanogr. 77, 1–29.

Lebreton, L., Slat, B., Ferrari, F., Sainte-Rose, B., Aitken, J., Marthouse, R., Hajbane, S., Cunsolo, S., Schwarz, A., Levivier, A., Noble, K., Debeljak, P., Maral, H., Schoeneich-Argent, R., Brambini, R., Reisser, J., 2018. Evidence that the Great Pacific Garbage Patch is rapidly accumulating plastic. Sci. Rep. 8, 4666. https://doi.org/10.1038/s41598-018-22939-w.

Liu, Y., Weisberg, R.H., 2011. Evaluation of trajectory modeling in different dynamic regions using normalized cumulative Lagrangian separation. J. Geophys. Res. Oceans 116. https://doi.org/10.1029/2010JC006837.

Lyard, F., Lefevre, F., Letellier, T., Francis, O., 2006. Modelling the global ocean tides: modern insights from FES2004. Ocean Dyn. 56, 394–415. https://doi.org/10.1007/s10236-006-0086-x.

Mann, K.H., Lazier, J.R., 2005. Dynamics of Marine Ecosystems: Biological-Physical Interactions in the Oceans. John Wiley & Sons.

Mantovani, C., Corgnati, L., Horstmann, J., Rubio, A., Reyes, E., Quentin, C., Cosoli, S., Asensio, J.L., Mader, J., Griffa, A., 2020. Best practices on high frequency radar deployment and operation for ocean current measurement. Front. Mar. Sci. 7.

Maraldi, C., Chanut, J., Levier, B., Ayoub, N., De Mey, P., Reffray, G., Lyard, F., Cailleau, S., Drévillon, M., Fanjul, E.A., Sotillo, M.G., Marsaleix, P., the Mercator Research and Development Team, 2013. NEMO on the shelf: assessment of the Iberia–Biscay–Ireland configuration. Ocean Sci. 9, 745–771. https://doi.org/10.5194/os-9-745-2013.

Mason, E., Ruiz, S., Bourdalle-Badie, R., Reffray, G., García-Sotillo, M., Pascual, A., 2019. New insight into 3-D mesoscale eddy properties from CMEMS operational models in the western Mediterranean. Ocean Sci. 15, 1111–1131. https://doi.org/10.5194/os-15-1111-2019.

McWilliams, J.C., 2016. Submesoscale currents in the ocean. Proceedings of the Royal Society A: Mathematical, Physical and Engineering Sciences 472, 20160117. https://doi.org/10.1098/rspa.2016.0117.

McWilliams, J.C., 2019. A survey of submesoscale currents. Geosci. Lett. 6, 3. https://doi.org/10.1186/s40562-019-0133-3.

Molcard, A., Piterbarg, L.I., Griffa, A., Özgökmen, T.M., Mariano, A.J., 2003. Assimilation of drifter observations for the reconstruction of the Eulerian circulation field. J. Geophys. Res. Oceans 108. https://doi.org/10.1029/2001JC001240.

Morales-Caselles, C., Viejo, J., Martí, E., González-Fernández, D., Pragnell-Raasch, H., González-Gordillo, J.I., Montero, E., Arroyo, G.M., Hanke, G., Salvo, V.S., Basurko, O.C., Mallos, N., Lebreton, L., Echevarría, F., van Emmerik, T., Duarte, C. M., Gálvez, J.A., van Sebille, E., Galgani, F., García, C.M., Ross, P.S., Bartual, A., Ioakeimidis, C., Markalain, G., Isobe, A., Cózar, A., 2021. An inshore–offshore sorting system revealed from global classification of ocean litter. Nat Sustain 4, 484–493. https://doi.org/10.1038/s41893-021-00720-8.

Muscarella, P., Carrier, M.J., Ngodock, H., Smith, S., Lipphardt, B.L., Kirwan, A.D., Huntley, H.S., 2015. Do assimilated drifter velocities improve Lagrangian predictability in an operational ocean model? Mon. Weather Rev. 143, 1822–1832. https://doi.org/10.1175/MWR-D-14-00164.1.

O'Reilly, J.E., Maritorena, S., Mitchell, B.G., Siegel, D.A., Carder, K.L., Garver, S.A., Kahru, M., McClain, C., 1998. Ocean color chlorophyll algorithms for SeaWiFS. J. Geophys. Res. Oceans 103, 24937–24953. https://doi.org/10.1029/98JC02160.

OSPAR Commission, 2000. Region IV: Bay of Biscay and Iberian Coast. The Commission.

Pereiro, D., Souto, C., Gago, J., 2018. Calibration of a marine floating litter transport model. J. Oper. Oceanogr. 11, 125–133. https://doi.org/10.1080/1755876X.2018.1470892.

Pereiro, D., Souto, C., Gago, J., 2019. Dynamics of floating marine debris in the northern Iberian waters: a model approach. J. Sea Res. 144, 57–66. https://doi.org/10.1016/j.seares.2018.11.007.

Pingree, R.D., Le Cann, B., 1992. Three anticyclonic slope water oceanic eDDIES (SWODDIES) in the Southern Bay of Biscay in 1990. Deep Sea Research Part A. Oceanographic Research Papers 39, 1147–1175. https://doi.org/10.1016/0198-0149(92)90062-X.

Poje, A.C., Özgökmen, T.M., Lipphardt, B.L., Haus, B.K., Ryan, E.H., Haza, A.C., Jacobs, G.A., Reniers, A.J.H.M., Olascoaga, M.J., Novelli, G., Griffa, A., Beron-Vera, F.J., Chen, S.S., Coelho, E., Hogan, P.J., Kirwan, A.D., Huntley, H.S., Mariano, A.J., 2014. Submesoscale dispersion in the vicinity of the Deepwater Horizon spill. Proc. Natl. Acad. Sci. 111, 12693–12698. https://doi.org/10.1073/pnas.1402452111.

Poulain, P.-M., Niiler, P.P., 1989. Statistical analysis of the surface circulation in the California current system using satellite-tracked drifters. J. Phys. Oceanogr. 19, 1588–1603. https://doi.org/10.1175/1520-0485(1989)019<1588:SAOTSC>2.0.CO;2.

Prants, 2022. Marine life at Lagrangian fronts. Prog. Oceanogr. 204, 102790 https://doi.org/10.1016/j.pocean.2022.102790.

Prants, Budyansky, M.V., Uleysky, M. Yu, 2014a. Lagrangian fronts in the ocean. Izv. Atmos. Ocean. Phys. 50, 284–291. https://doi.org/10.1134/S0001433814030116.

Prants, Budyansky, M.V., Uleysky, M. Yu, 2014b. Identifying Lagrangian fronts with favourable fishery conditions. Deep-Sea Res. I Oceanogr. Res. Pap. 90, 27–35. https://doi.org/10.1016/j.dsr.2014.04.012.

Rodríguez-Díaz, L., Gómez-Gesteira, J.L., Costoya, X., Gómez-Gesteira, M., Gago, J., 2020. The Bay of Biscay as a trapping zone for exogenous plastics of different sizes. J. Sea Res. 163, 101929 https://doi.org/10.1016/j.seares.2020.101929.

Rubio, A., Reverdin, G., Fontán, A., González, M., Mader, J., 2011. Mapping near-inertial variability in the SE Bay of Biscay from HF radar data and two offshore moored buoys. Geophys. Res. Lett. 38 https://doi.org/10.1029/2011GL048783.

Rubio, A., Caballero, A., Orfila, A., Hernández-Carrasco, I., Ferrer, L., González, M., Solabarrieta, L., Mader, J., 2018. Eddy-induced cross-shelf export of high Chl-a coastal waters in the SE Bay of Biscay. Remote Sens. Environ. 205, 290–304. https://doi.org/10.1016/j.rse.2017.10.037.

Rubio, A., Manso-Narvarte, I., Caballero, A., Corgnati, L., Mantovani, C., Reyes, E., Griffa, A., Mader, J., 2019. The seasonal intensification of the slope Iberian Poleward Current. In: Copernicus Marine Service Ocean State Report. Journal of Operational Oceanography, 3, pp. 13–18. https://doi.org/10.1080/1755876X.2019.1633075.

Rubio, A., Hernández-Carrasco, I., Orfila, A., González, M., Reyes, E., Corgnati, L., Berta, M., Griffa, A., Mader, J., 2020. A Lagrangian approach to monitor local particle retention conditions in coastal areas. Copernicus Marine Service Ocean State Report 54–59.

Ruiz, I., Basurko, O.C., Rubio, A., Delpey, M., Granado, I., Declerck, A., Mader, J., Cózar, A., 2020. Litter windrows in the South-East Coast of the Bay of Biscay: an ocean process enabling effective active fishing for litter. Front. Mar. Sci. 7.

Ruiz, I., Rubio, A., Abascal, A.J., Basurko, O.C., 2022. Modelling floating riverine litter in the south-eastern Bay of Biscay: a regional distribution from a seasonal perspective. Ocean Sci. 18, 1703–1724. https://doi.org/10.5194/os-18-1703-2022.

Rußwurm, M., Venkatesa, S.J., Tuia, D., 2023. Large-scale detection of marine debris in coastal areas with Sentinel-2. iScience 26, 108402. https://doi.org/10.1016/j.isci.2023.108402.

Sentchev, A., Yaremchuk, M., 2015. Monitoring tidal currents with a towed ADCP system. Ocean Dyn. 66 https://doi.org/10.1007/s10236-015-0913-z.

Skamarock, W.C., Klemp, J.B., Dudhia, J., Gill, D.O., Liu, Z., Berner, J., Wang, W., Powers, J.G., Duda, M.G., Barker, D.M., 2019. A Description of the Advanced Research WRF Version 4. NCAR tech. note ncar/tn-556+ str 145.

Solabarrieta, L., Rubio, A., Castanedo, S., Medina, R., Charria, G., Hernández, C., 2014. Surface water circulation patterns in the southeastern Bay of Biscay: new evidences from HF radar data. Cont. Shelf Res. 74, 60–76. https://doi.org/10.1016/j.csr.2013.11.022.

Solabarrieta, L., Rubio, A., Cárdenas, M., Castanedo, S., Esnaola, G., Méndez, F.J., Medina, R., Ferrer, L., 2015. Probabilistic relationships between wind and surface water circulation patterns in the SE Bay of Biscay. Ocean Dyn. 65, 1289–1303. https://doi.org/10.1007/s10236-015-0871-5.

Solabarrieta, L., Frolov, S., Cook, M., Paduan, J., Rubio, A., González, M., Mader, J., Charria, G., 2016. Skill assessment of HF radar–derived products for Lagrangian simulations in the Bay of Biscay. J. Atmos. Ocean. Technol. 33, 2585–2597. https://doi.org/10.1175/JTECH-D-16-0045.1.

Stock, A., Subramaniam, A., Van Dijken, G.L., Wedding, L.M., Arrigo, K.R., Mills, M.M., Cameron, M.A., Micheli, F., 2020. Comparison of cloud-filling algorithms for marine satellite data. Remote Sens. 12, 3313. https://doi.org/10.3390/rs12203313.

Suara, K., Khanarmuei, M., Ghosh, A., Yu, Y., Zhang, H., Soomere, T., Brown, R.J., 2020. Material and debris transport patterns in Moreton Bay, Australia: the influence of Lagrangian coherent structures. Sci. Total Environ. 721, 137715 https://doi.org/10.1016/j.scitotenv.2020.137715.

Suaria, G., Berta, M., Griffa, A., Molcard, A., Özgökmen, T.M., Zambianchi, E., Aliani, S., 2022. Dynamics of transport, accumulation, and export of plastics at oceanic fronts. In: Belkin, I.M. (Ed.), Chemical Oceanography of Frontal Zones, the Handbook of Environmental Chemistry. Springer, Berlin, Heidelberg, pp. 355–405. https://doi.org/10.1007/698_2021_814.

Sun, L., Penny, S.G., 2019. Lagrangian data assimilation of surface drifters in a double-gyre ocean model using the local ensemble transform Kalman filter. Mon. Weather Rev. 147, 4533–4551. https://doi.org/10.1175/MWR-D-18-0406.1.

Taylor, G.I., 1922. Diffusion by continuous movements. Proc. Lond. Math. Soc. 2, 196–212.

van Sebille, E. van, Wilcox, C., Lebreton, L., Maximenko, N., Hardesty, B.D., Franeker, J. A. van, Eriksen, M., Siegel, D., Galgani, F., Law, K.L., 2015. A global inventory of small floating plastic debris. Environ. Res. Lett. 10, 124006 https://doi.org/10.1088/1748-9326/10/12/124006.

van Sebille, E. van, Aliani, S., Law, K.L., Maximenko, N., Alsina, J.M., Bagaev, A., Bergmann, M., Chapron, B., Chubarenko, I., Cózar, A., Delandmeter, P., Egger, M., Fox-Kemper, B., Garaba, S.P., Goddijn-Murphy, L., Hardesty, B.D., Hoffman, M.J., Isobe, A., Jongedijk, C.E., Kaandorp, M.L.A., Khatmullina, L., Koelmans, A.A., Kukulka, T., Laufkötter, C., Lebreton, L., Lobelle, D., Maes, C., Martinez-Vicente, V., Maqueda, M.Á., Poulain-Zarcos, M., Rodríguez, E., Ryan, P.G., Shanks, A.L., Shim, W.J., Suaria, G., Thiel, M., Bremer, T.S. van den, Wichmann, D., 2020. The physical oceanography of the transport of floating marine debris. Environ. Res. Lett. 15, 023003 https://doi.org/10.1088/1748-9326/ab6d7d.

Xing, Q., Yu, H., Wang, H., Ito, S., 2023. An improved algorithm for detecting mesoscale ocean fronts from satellite observations: detailed mapping of persistent fronts around the China Seas and their long-term trends. Remote Sens. Environ. 294, 113627 https://doi.org/10.1016/j.rse.2023.113627.

Yaremchuk, M., Sentchev, A., 2009. Mapping radar-derived sea surface currents with a variational method. Cont. Shelf Res. 29, 1711–1722. https://doi.org/10.1016/j.csr.2009.05.016.

Zainuddin, M., Kiyofuji, H., Saitoh, K., Saitoh, S.-I., 2006. Using Multi-sensor Satellite Remote Sensing and Catch Data to Detect Ocean Hot Spots for Albacore (*Thunnus alalunga*) in the Northwestern North Pacific. Deep Sea Research Part II: Topical Studies in Oceanography, Top Predator "Hot Spots" in the North Pacific, 53, pp. 419–431. https://doi.org/10.1016/j.dsr2.2006.01.007.

Zambianchi, E., Trani, M., Falco, P., 2017. Lagrangian transport of marine litter in the Mediterranean Sea. Frontiers in Environmental Science 5.